Nonlinear viscoelasticity of Filamentous Fungal Biofilms of *Neurospora discreta*

Aiswarya N M[a], Shamas Tabraiz[b,c], Himani Taneja[b,e], Asma Ahmed[b,d], Aravinda Narayanan R[a*]

[a]Department of Physics, Birla Institute of Technology and Science Pilani, Hyderabad Campus, India

[b]Section of Natural and Applied Sciences, Canterbury Christ Church University, UK

[c]Department of Civil and Environmental Engineering, Imperial College London, South Kensington Campus, Imperial College Road, SW7 2BU, London, UK

[d]Department of Chemical and Environmental Engineering, Faculty of Engineering, University of Nottingham, Nottingham NG7 2RD

[e]Liverpool School of Tropical Medicine, Pembroke Place, Liverpool, L3 5QA UK

*Corresponding author: raghavan@hyderabad.bits-pilani.ac.in

Abstract

The picture of bacterial biofilms as a colloidal gel composed of rigid bacterial cells protected by extracellular crosslinked polymer matrix has been pivotal in understanding their ability to adapt their microstructure and viscoelasticity to environmental assaults. This work explores if an analogous perspective exists in fungal biofilms with long filamentous cells. To this end, we consider biofilms of the fungus *Neurospora discreta* formed on the air-liquid interface, which has shown an ability to remove excess nitrogen and phosphorous from wastewater effectively. We investigated the changes to the viscoelasticity and the microstructure of these biofilms when the biofilms uptake varying concentrations of nitrogen and phosphorous, using large amplitude oscillatory shear flow rheology (LAOS) and field-emission scanning electron microscopy (FESEM), respectively. A distinctive peak in the loss modulus (G") at 30-50% shear strain is observed, indicating the transition from an elastic to plastic deformation state. Though a peak in G" has been observed in several soft materials, including bacterial biofilms, it has eluded interpretation in terms of quantifiable microstructural features. The central finding of this work is that the intensity of the G" peak, signifying resistance to large deformations, correlates directly with the protein and polysaccharide concentrations per unit biomass in the extracellular matrix and inversely with the shear-induced changes in filament orientation in the hyphal network. These correlations have implications for the rational design of fungal biofilms with tuneable mechanical properties.

Keywords: Fungal biofilm, mechanics, viscoelasticity, strain overshoot, LAOS, filament orientation

1. Introduction

Microorganisms like bacteria and yeast thrive on almost every surface that contains even trace amounts of nutrients and moisture, ranging from kitchen countertops and dental surfaces to industrial and medical equipment.[1] Some of these microbial species can form a cluster of cells, which secrete extracellular polymeric substances (EPS) to ensconce themselves to form biofilms that enable them to withstand environmental perturbations.[2] Such fortification helps biofilms to spread infectious diseases[3] and corrode industrial equipment.[4] In response to the environmental perturbations, the biofilms alter the EPS biochemical composition, modifying their viscoelasticity. Therefore, the main interest in studying biofilm material properties has been understanding biofilms' adhesion to surfaces, especially bacterial biofilms.[5–10] However, some biofilms aid in preventing infection caused by pathogens in the plant rhizosphere, treat wastewater, and process food.[11,12] The non-pathogenic filamentous fungi – *Neurospora discreta* – whose biofilms are the subject of this study, degrade complex lignin found in agricultural residues,[13] a useful property for treating wastewater from the paper and pulp industry.

Until a decade ago, it was not obvious that a single filamentous fungal cell – hypha – could form a biofilm; it extends at its tip by taking up nutrients and branches to create an interconnected hyphal network; the nuclear material flows through the entire network.[14,15] Bacterial and filamentous fungal cells significantly differ in how they seek nutrients. Bacterial cells can move due to the local forces,[16] whereas filamentous fungal cells use the local forces to grow in length and branch out.[17] In the case of filamentous fungi, which have been considered cell factories for an array of industrial products, including enzymes, organic acids, secondary metabolites, vitamins, composite materials, and textiles,[17] there is a dearth of studies providing insights on the rheological behavior of their biofilms.[18,19]

A recent report indicated that six of the nine planetary boundaries that make the world habitable have been breached.[20] One of them is the excessive amount of nutrients - nitrogen and phosphorus - that run into wastewater, affecting the ecological balance. A previous study showed that porous biofilms of *N. discreta* can simultaneously and effectively remove carbon, nitrogen, and phosphorous from synthetic wastewater.[19,21] In this context, it is imperative to understand the modifications to the biofilms' viscoelasticity and microstructure due to the uptake of the excess nutrients for their potential application as membranes.

To comprehend the structure-rheology relationship of a biofilm, it helps to identify its components and their function.[22] Two complimentary perspectives can be considered: (1) *Static picture*: The microbial cell has a rigid exoskeleton that provides structural integrity. The extracellular matrix polymers secreted by the cells ensure the formation of a close-knit viscoelastic solid. The EPS primarily consists of biopolymers: extracellular DNA, polysaccharides, proteins, and nucleic acids that are topologically entangled and crosslinked by accessory proteins and multivalent cations.[2] The mechanical softness of biofilms, with an elastic modulus of a few kPa, can also be attributed to water held in micro and nanopores that accounts for nearly ninety percent of the weight of a biofilm.[19] (2) *Dynamic picture*: Spatial gradients in nutrient concentration influence metabolic activity and cellular phenotype expression.[23] During the biofilm growth, external stimuli such as varying the complexity of the carbon source,[24] agitating the growth reactor culture medium,[19] and depleting nutrients can all affect spatial gradients,[25] increasing the EPS production to the extent that a biofilm can transform its microstructure and rheological properties to that of a predominantly solid state from a liquid state. As the biofilm structurally evolves, the spatial gradients in nutrient concentration cause local variations in extracellular matrix composition, generating local forces [26] to spread the biofilm further.

In soft materials such as biofilms, even a small strain amplitude (~ 1%) can cause large structural rearrangements and consequently provide a nonlinear rheological response.[27,28] In large amplitude oscillatory shear rheology (LAOS), a harmonic strain input to a material produces a nonlinear stress response at higher strain amplitudes; the higher harmonics present in the response contain information on nonlinear rheological phenomena such as strain stiffening and shear thinning.[29] Probing complex fluids using LAOS has led to the identification of four types of materials based on variations in storage modulus (G') and loss modulus (G"). They are strain thinning (Type I), strain hardening (Type II), weak strain overshoot (Type III), and strong strain overshoot (Type IV). [30] The few reports that exist on LAOS on biofilms show that biofilms belong to Type III, characterized by a decrease of G' at higher strains, and G" that peaks at intermediate strains (10-100%) - weak overshoot - and then continuously decreases at even higher strains.[31–33] The peak in G" is associated with a yielding transition from an elastic-like deformable state to a fluid-like state.[34] While various materials exhibit a peak in G", the *challenge* has been quantitatively correlating it with specific microstructural features.[35]

A material standard whose rheological behavior is like biofilms and exhibits type III behavior is xanthan gum, an exopolysaccharide produced by the bacterium *Xanthomonas Campestris*: In

this case, the peak in G" is attributed to the presence of charged groups on the long side chains forming a soft structural complex with neighboring polymers, to increase viscosity and resist deformation.[30] Jana et al. used LAOS to characterize biofilms of four different bacterial species. A peak in G" was observed for all the species at a different strain amplitude with distinctly different elastic energy dissipation characteristics.[31] However, their rheological behavior could not be linked to specific microstructural features, as the biofilms were from different species. To unravel the specific role of various components of the EPS in determining the biofilm's nonlinear viscoelastic behavior, Zhang et al. systematically studied bacterial biofilms of *Vibrio cholerae* devoid of one or more of the components of the EPS. One of the key findings was that accessory proteins, which enable cell-to-cell adhesion and crosslink the polysaccharide polymer network, help the biofilm to withstand large shear forces.[32] While the research on biofilm mechanics to date has primarily focussed on bacterial biofilms[36], the following questions on the largely unexamined filamentous fungal biofilm mechanics are pertinent: (1) Is the nonlinear viscoelastic behavior of a fungal biofilm similar to bacterial biofilms in that features like weak-strain overshoot is observed? (2) If so, can the changes in viscoelasticity be ascribed to specific changes in the EPS composition or the hyphal network? As an aside, LAOS of bacterial biofilms was performed on composite biofilms obtained by pooling together scraped pieces from a solid substrate, indicating biofilm testing challenges. [37,38]

In this work, we study the influence of EPS and the hyphal network on fungal biofilm mechanics, which is probed using LAOS. For this purpose, we grew biofilms of filamentous fungi *N. discreta* on an air-liquid interface: This enabled harvesting of the biofilm as a whole, which assisted in overcoming the biofilm testing challenge mentioned above. We varied EPS and regulated the polarized growth of the hyphal network by growing the biofilms in synthetic wastewater containing varying concentrations of nitrogen and phosphorous. In the first part, we present results from rheological studies and identify a parameter that quantifies resistance to large shear deformation. Then, we show the results and analysis of imaging of the hyphal network before and after the most extensive shear deformation. Finally, we deduce relationships between the microstructure and non-linear viscoelastic behavior of the biofilms.

2. Experimental Methods

2.1. Sample preparation

Strain and inoculum preparation: The filamentous fungal strains of *N. discreta* were isolated from Subabul tree and grown on potato dextrose plates for three days at 30°C. **Figure S1** shows

the phylogenetic tree derived from the gene sequence of the 18S rRNA internal transcribed spacer (ITS) received from the CSIR-Institute of Microbial Technology in Chandigarh, India. Cells were then suspended in Vogel's minimum medium (30 mL) devoid of KH_2PO_4, NH_4NO_3, and sucrose for inoculation. Centrifugation of fungal spore and filament suspension was carried out at 5000xg for 5 minutes. The pellets obtained after discarding the supernatant were suspended again in Vogel's media. Filaments were filtered out using non-sterile Nylon syringe filter (0.45 μ)- Fisherbrand™, and a spore solution was prepared for inoculation.

Biofilm formation: Biofilms were grown in modified Vogel's media – synthetic wastewater - in the air-liquid interface.[21] Nitrogen concentration was varied by altering the NH_4NO_3 amount, and phosphorus concentration was controlled using KH_2PO_4. The nutrient concentrations in the nitrogen and phosphorus trial are given in **Table 1**. After 7 days of growth, the biofilms were harvested by sliding a flat spatula under the biofilm, lifting it off the water surface, and removing it from the reactor (**Figure S2**a). The harvested biofilms were submerged in 70% isopropyl alcohol (IPA) to prevent further microbial growth and stored at 4 ^{0}C for further characterization.

Table 1: Nutrient concentrations in the nitrogen and phosphorus trials [21]

Concentration in solution (g.L^{-1})			
Reactor	**C**	**N**	**P**
Nitrogen trial			
NA	8.41	0.70	1.13
NB	8.41	0.35	1.13
NC	8.41	0.175	1.13
ND	8.41	0.044	1.13
Phosphorus trial			
PA	8.41	0.70	1.13
PB	8.41	0.70	0.564
PC	8.41	0.70	0.282
PD	8.41	0.70	0.070
PE	8.41	0.70	0.017

EPS extraction:

For EPS extraction, a 10ml solution was prepared by adding 0.22% formaldehyde and 8.5% sodium chloride. A section of the biofilm was first drained on blue tissue paper to remove the

excess water from the samples, then excised, weighed, and added to the solution. The biofilm samples were *not* treated with IPA before this process. The solution was incubated for 3 hours at 4 ℃, followed by 10000 × *g* centrifugation for 10 minutes. The resulting supernatant was filtered using a 0.45 µm filter (Fisherbrand™) and stored at 20 °C for further analysis. The dinitro salicylic acid (DNS) reagent method was used to measure the concentration of polysaccharides in the EPS.[21] A colorimetric kit (77371, Sigma Aldrich, UK) was used to quantify the protein concentration in the EPS following the manufacturer's instructions.

2.2. Microscopic studies

A biofilm is structurally heterogeneous. Therefore, to draw structure-property correlations of biofilms grown under different nutrient concentrations, the biofilm samples for FESEM (Apreo S, FEI) imaging and rheological testing were always cut from the edge of the circularly shaped biofilm. The reason for this choice is during the biofilm growth in the conical flask, the edges of the biofilm grew in attachment to the glass surface; therefore, the microstructure around the circular edge can be assumed to be consistent[9]. Imaging of the hyphal network of biofilms was carried out at 25°C on a circular piece of biofilm (8mm diameter) called 'before rheology' images. Another piece of biofilm (8mm diameter) was cut for an LAOS test. After the completion of the test, this piece of the biofilm was subjected to FESEM imaging, which is termed 'after rheology' images. The imaging was done at 1500X, 2500X, and 5000X magnifications. *ImageJ* software was used to analyze the filament characteristics.[40] We converted 2500X magnification SEM images to an 8-bit binary image for filament orientation distribution analysis. Furthermore, we employed two features of the *OrientationJ* plugin within *ImageJ* software to obtain the following: 1) *OrientationJ distribution* wizard to extract the distribution of filaments at different angles and 2) *OrientationJ Analysis* wizard for HSB color-coded map of orientation angles of filaments.[41] The obtained distribution curves were smoothed using the 5-point Savitzky-Golay method[42] to remove noise peaks. For instance, see the noise peaks in the calibration curve in **Figure S8**. The multiple Gaussian peak fitting module in the Origin Pro software was used to derive the area under each peak, representing the proportion of filaments oriented at a certain angle. Later, in section 3. 2, we define a dimensionless quantity called the orientation complexity function (OCF) to quantify the changes in filament orientation of biofilms due to large deformations. For this purpose, the dried biofilm is imaged at three different regions in each replicate.

2.3. Large amplitude oscillatory shear tests

Rheological studies: LAOS testing was carried out using a combined motor transducer rheometer (Anton Paar MCR 302 supported by RheoCompass software). As a control experiment, for comparing the intensity of the weak strain overshoot defined as $\beta = \frac{G'_{peak}}{G'_{plateau}}$, the LAOS test was performed on xanthan gum gel (4 wt.%), using 25 mm diameter parallel plate geometry, at 1 rad/sec frequency by varying the shear strain amplitude between 1%-1000%. We obtained $\boldsymbol{\beta}$ = 2.12 ± 0.03. This value is comparable to the reported values in the literature for xanthan gum prepared under similar conditions.[43] We also performed LAOS tests on xanthan gum (4 wt.%) submerged in IPA for a day to confirm that IPA does not affect the rheological properties of the samples (**Figure S3**). The LAOS test on fungal biofilms was performed using parallel plate geometry (8 mm diameter). The biofilms were taken out of storage (4 ^{0}C) just before the LAOS tests and were cut to a circular shape of diameter 8 mm using a custom-made tool and loaded on the parallel plate, ensuring that there were no folds, and the sample was intact. **Figure S2**b shows the biofilm sandwiched between two parallel plates just before the LAOS test. The gap between the plates was kept constant for each sample throughout the experiment, and it varied between 0.08-0.3mm depending on the sample thickness. The samples were subjected to a sinusoidal shear strain sweep between 0.1%-500% at 1Hz, 2Hz, and 3Hz. The tests were conducted at a constant temperature of 25 °C and took around 15 minutes to finish. The samples that underwent LAOS test were stored at 4 ^{0}C for SEM imaging. It is to be noted that, in the parallel plate geometry the deformation strain field varies radially from the center of the sample[39]. To ensure that we are comparing samples subjected to the same deformation field, we imaged all the samples on the circular edge of the sample after drying in a vacuum (0.2 bar) for 48 hours at room temperature. The raw data obtained after completing the tests were processed using *MITlaos*, software.[44] LAOS data was processed by assuming a maximum of three harmonics. The magnitude of I_3/I_1 was approximately 10 percent, where I_3 is the intensity of the third harmonic, and I_1 is the intensity of the fundamental harmonic.[45]

Monitoring sample slip: In rheometry, usually sandblasted rough plate surfaces are used to prevent slipping of samples.[46] However, we did not use it because a roughened surface could puncture the biofilm, leaving the possibility of water oozing out. Water is an essential

component contributing to the mechanical property.[19] We monitored the sample slipping visually and used the following criterion as a precaution to discard data at higher strain amplitudes and frequencies at which the biofilms are more likely to slip. The criterion is that the sample torque should be greater than the instrument torque.[38] According to Anton Paar, the data is acceptable if this ratio exceeds 0.5. We computed the ratio of sample torque to instrument inertia torque for each sample and discarded those data that failed this criterion, occurring mostly at higher strain amplitudes and frequencies greater than 1Hz (**Figure S4, S5, and S6**).

2.4. Statistical analysis:

Heat maps were constructed to visualize Pearson's correlation between the rheological and biochemical composition of the EPS and the change in the orientation distribution of filamentous cells of the biofilms. This analysis utilized R software's "metan" package (version 4.3.1).

3. Results and discussions

3.1. Response to large oscillatory shear

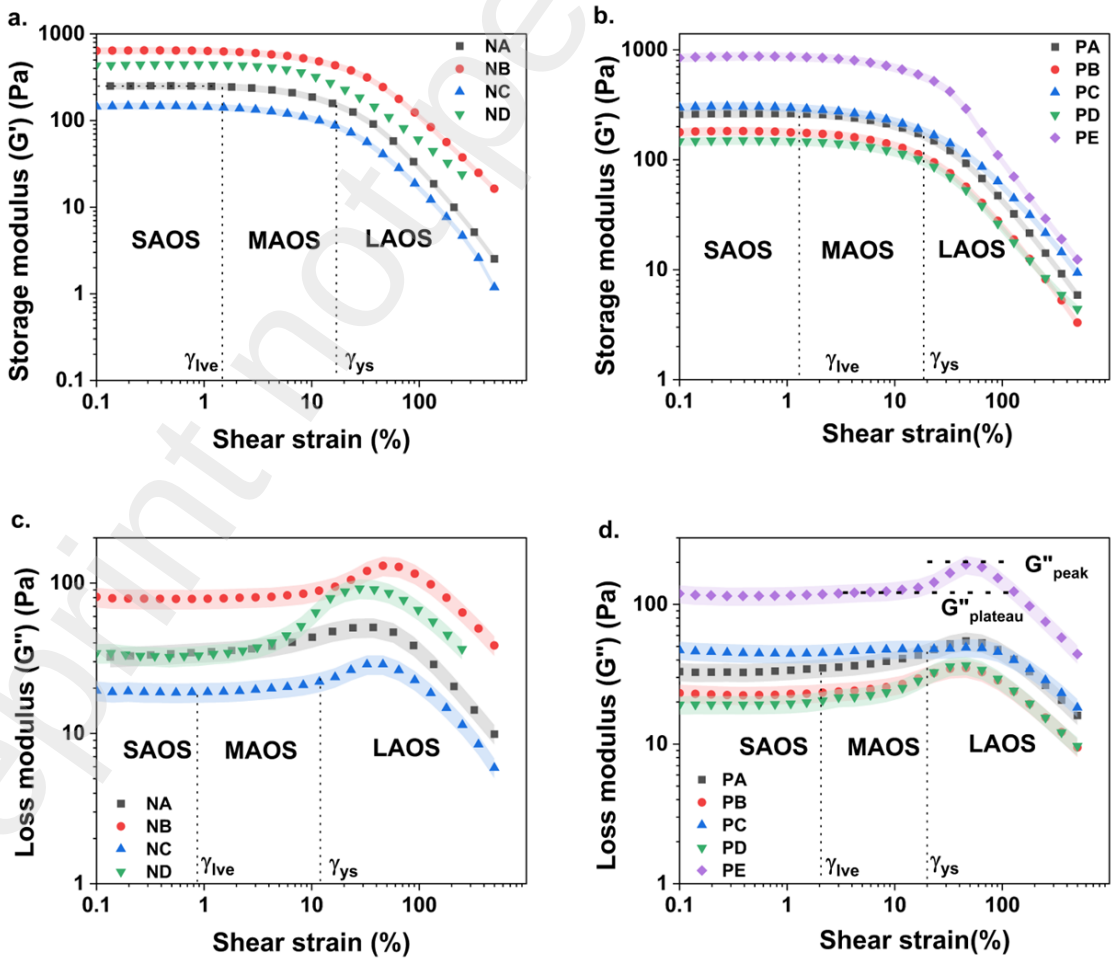

Figure 1. Storage modulus (G') and loss modulus (G") as a function of shear strain percent for the fungal biofilms. Plots (a) and (b) show G' for nitrogen and phosphorous, respectively. Plots (c) and (d) show G" for nitrogen, and phosphorous trials, respectively. The instrument error band (shaded region) corresponds to one standard deviation (n=3).

To understand the viscoelasticity of the biofilms, G', the elastic component, which is related to the average energy stored over a cycle [47]; and G", the viscous component, associated with the average energy dissipated over a cycle as heat, is plotted as a function of shear strain for the nitrogen trial and phosphorus trials, in **Figure 1**. As shear strain increases, the shear stress increases proportionally, marked by a constant G'. This region is known as the linear viscoelastic regime (LVE), synonymous with the small amplitude oscillatory shear region (SAOS). Upon further increase in strain, G' decreases nonlinearly in the medium amplitude oscillatory region (MAOS), and at even larger strains, in the LAOS region, G' decreases more rapidly. The nonlinear decrease in storage modulus at higher strains implies strain-softening behavior. The LVE regime (G') storage modulus for these biofilms is comparable to other soft materials,[27], which is between 100 Pa – 1000 Pa. For all the biofilms, γ_{LVE}, the critical strain demarcating SAOS and MAOS regions, is 0.9%-2%, comparable to bacterial biofilms and xanthan gum gel.[31,48] The transition strains, γ_{LVE} and γ_{ys} **(Figure 1** a, b **)**, were obtained by mathematically differentiating storage modulus with respect to shear strain. The magnitude of G" is lower than that of G' in the LVE region as expected for a viscoelastic solid. During strain sweep, G" remains constant well into the MAOS regime, peaks (weak strain overshoot) in the LAOS regime, and decreases at even larger strains. A similar peak in G" has been observed in bacterial biofilms.[31–33,49,50] In nitrogen and phosphorus trials, the G" peak occurs between 30%-50% shear strain **(Figure 1** c, d**).**

Furthermore, we noticed that the magnitude of the peak in G" varied with nitrogen and phosphorus concentrations: We define the dimensionless parameter, $\beta = {G"_{peak}}/{G"_{plateau}}$, which serves as a nonlinear rheological measure for correlating with parameters describing the microstructure later in this article. To understand the reasons for probing nonlinear viscoelasticity, we plotted normalized shear strain and shear stress using yield strain, γ_{ys}, and the corresponding yield stress, σ_{ys} (**Figure S7** a, b**).** Data for both nitrogen and phosphorus trials collapse onto a straight line for the normalized shear strain and shear stress values till $\gamma = \gamma_{ys}$; for greater strains, we observe deviations caused by differences in the biochemical composition of the biofilms, resulting in varying rates of strain softening.

LAOS probes material states continuously as the strain sweeps, and the resultant data is presented visually through Lissajous Bowditch (L-B) plots. The non-sinusoidal stress signal due to a sinusoidal strain signal is decomposed into an elastic L-B plot where stress is plotted against strain and a viscous L-B plot where stress is plotted against strain rate. We measured stress response at 25 different strain values. We chose a strain value each in the SAOS, MAOS, and LAOS regimes and presented the L-B plots in **Figure 2**, which show the evolution in structural deformation seen through variation in the geometrical shapes of the closed curves. In the SAOS regime, the elastic L-B plots show a rotated elliptical shape because, in a cycle, the stress and strain are nearly in phase. In the elastic L-B plot, the area enclosed by the curve is proportional to energy dissipation; the most extensive dissipation occurs in the LAOS regime (**Figure 2** a-c). The viscous L-B plots show a nearly circular shape in the SAOS regime (elastic nature) because the stress and strain rate differ in phase by 90^0. In the LAOS regime, the closed curves acquire a sigmoidal shape (viscous nature) (**Figure 2** d-f). These findings are similar to those seen with bacterial biofilms.[31,32] We observed self-intersecting loops at very high strains (500%) in viscous L-B plots, interpreted as arising due to stress overshoot,[51], which will not concern us in this article.

The L-B plots provide information regarding nonlinear deformations due to an oscillatory strain that operates between a certain maximum and minimum shear strain amplitude. The resultant material deformations are quantified using two dimensionless indices. They are the intra-cycle strain stiffening index, $S = \frac{G'_L - G'_M}{G'_L}$, and the intra-cycle shear thickening index, $T = \frac{\eta'_L - \eta'_M}{\eta'_L}$.[47] To understand the motivation for these indices, consider the elastic LB plot of shear strain 37.2 % **(Figure 2**b**)**. The material state moving from point *a* to *b* in a clockwise direction is equivalent to shear strain increasing from zero to 0.372, due to which shear stress also increases, causing a mild strain stiffening behavior. Note that at point *a*, there is a finite stress for zero shear strain, the result of an accumulation from previous cycles at smaller shear strain amplitudes. Now, when we move from point *b* to *c*, the shear strain decreases to zero, followed by a decrease in stress. The dashed lines in **Figure 2**b denote the shear modulus at the largest (G'_L) and shear modulus at zero strain (G'_M); the difference between these two moduli measures the intra-cycle stiffening of the sample. Similarly, the intra-cycle shear thickening index is defined as the difference between the slopes η'_L (maximum strain rate) and η'_M (zero strain rate) in the viscous L-B plots. So, if $S > 0$, it implies strain stiffening behavior; $S < 0$ indicates strain softening;

$S = 0$ pertains to linear elastic behavior. Similarly, $T > 0$ and $T < 0$ imply shear thickening and shear thinning behavior, respectively, and $T = 0$ corresponds to linear viscous behavior.

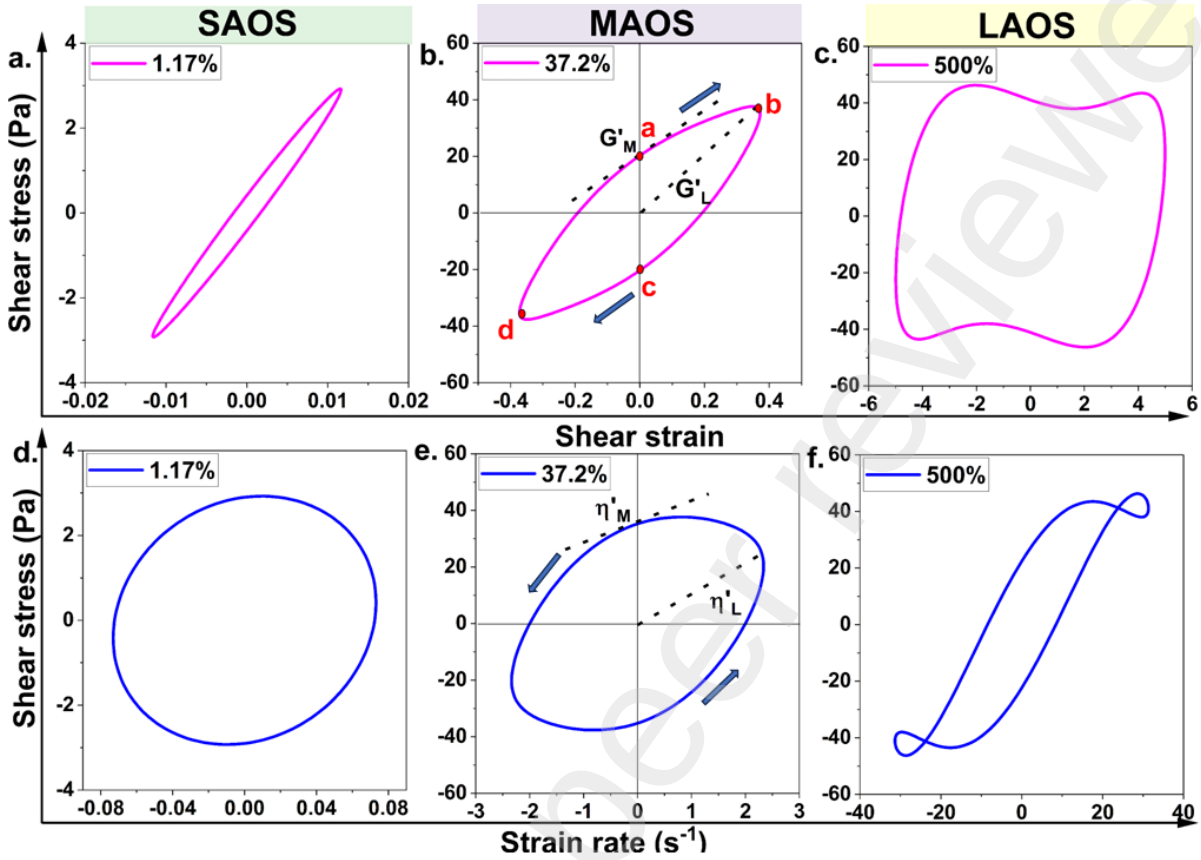

Figure 2. Geometrical representation of shear rheology in the SAOS, MAOS, and LAOS regimes for a typical fungal biofilm (NA). Plots (a), (b), and (c) show elastic L-B curves, and plots (d), (e), and (f) show the viscous L-B curves.

We observe that biofilms in the nitrogen and phosphorous trials maintain intra-cycle elasticity ($S = 0$) well into the MAOS regime and then strain stiffen ($S > 0$) in the LAOS regime (**Figure 3** a, b). On the contrary, the biofilms shear thicken ($T > 0$) at smaller shear strains until strains in the MAOS regime: This 'early' departure from linearity (**Figure 3** c, d) suggests that the nonlinear rheology in these fungal biofilms is triggered by their viscous nature, similar to other polysaccharide-based gels[52]. The peak in T occuring in the range $10\% < T < 100\%$, is another manifestation of the weak strain overshoot. In the LAOS regime, the biofilms exhibit shear thinning behavior ($T < 0$) (**Figure 3** c, d).

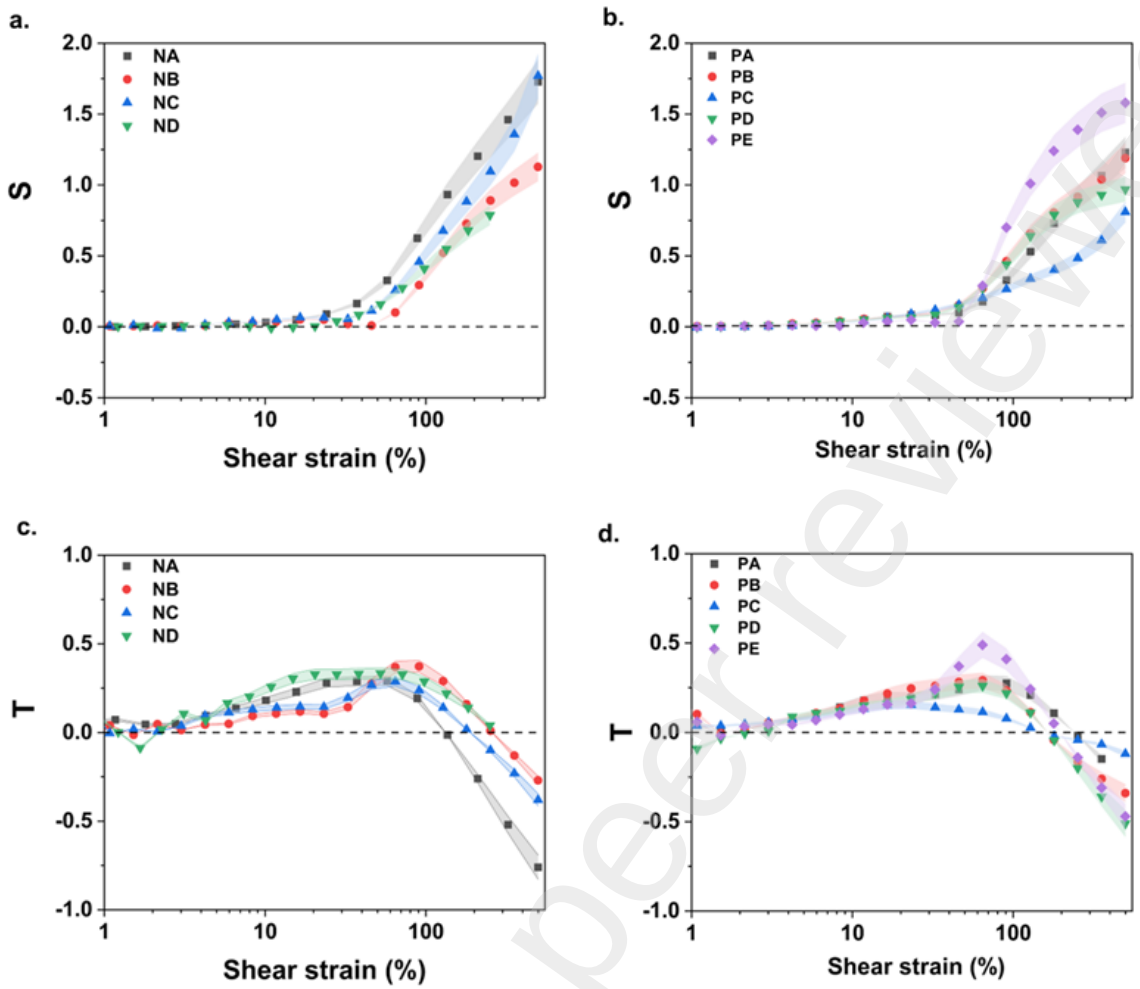

Figure 3. Intracycle strain stiffening (*S*) and shear thickening (*T*) indices as a function of shear strain. Plots (a) and (b) show *S* of the nitrogen trial and phosphorus trial, respectively, and plots (c) and (d) show *T* of the nitrogen trial and phosphorus trial, respectively. The instrument error band (shaded region) corresponds to one standard deviation (n=3).

3.2. Filament orientation – Characterization of microstructure

By varying the nutrient concentration, EPS production, filament length and filament orientation can be influenced.[19,24] The FESEM images show one of the major components of the microstructure - hyphal network and the pores between them (**Figure 4**a). In our previous study, we observed that depletion of the nutrients - nitrogen and phosphorous - caused fungal hyphae to grow in length in search of nutrients and become thicker monotonically, while the composition of EPS varies non-monotonically.[21] In materials, such as liquid crystals, and actin networks, mesophase orientational order is known to couple with polymer matrix to influence the mechanical properties.[53,54] To explore the connection between extracellular polymer matrix

and the hyphal network, we imaged the biofilms before rheology (**Figure 4**a) and after the largest shear strain (**Figure 4**b). In the FESEM images, we analyze the orientation of at least 12,000 filaments (Please look at the maximum magnitude in **Figure 4**).

Here, we discuss the general results by considering the sample PC as an example. We extracted the filament orientation distribution from the images: Before rheology, the sample had a nearly symmetrical distribution with a sharp peak at 0^0 and broader peaks centered around -45^0 and $+45^0$ (**Figure 4**c). After rheology, while the sample continues to have a sharp peak at 0^0 and a broader peak around -45^0, the area of peak around $+45^0$ significantly increased implying a greater number of filaments oriented in that direction (**Figure 4**d). Before the analysis, we calibrate the software (*OrientationJ*) by extracting the filament orientation distribution using a customized image with predefined angles (**Figure S8**). The orientation distribution was fit, assuming that the area under the curve is the sum of the areas of an optimum number of peaks pertaining to each orientation. The peaks were fit to a Gaussian function. Furthermore, to quantify the changes in the filament orientation in the hyphal network due to mechanical deformation, we define a dimensionless quantity, the filament orientation complexity function (OCF), which is like the definition of entropy in statistical mechanics.[55]

$$OCF = -\sum_{i=1}^{N} \frac{A_i}{A_T} \ln \frac{A_i}{A_T} \qquad (1)$$

A_i is the area enclosed by the Gaussian curve about a particular orientation; A_T is the total area under the orientation distribution curve, and N corresponds to the number of Gaussian peaks. The ratio $\frac{A_i}{A_T}$ is the relative measure of filaments oriented at a certain angle. This function succinctly provides a number that indicates the diversity in filament orientation and their population. To elaborate, if the filaments orient along the same direction, then OCF would be zero. This is equivalent to observing a single Gaussian distribution of filament orientations centered around an angle. At the other extreme, OCF will be at its maximum if the filament population is equally distributed among all possible orientations – a perfect random angular distribution. It is to be noted that a similar measure has been defined in other contexts as well.[55,56] In our work, we observe more than one Gaussian peak, and the area under them is not equal (**Figure 4**c), indicating that the orientation of filaments is neither completely anisotropic nor randomly oriented. We know that filamentous cell undergo directed growth and rheological deformation can change the orientations.[17] Shear-induced changes in the distribution of filament orientation are therefore, quantified using the following:

$$|\Delta OCF| = |OCF_{After} - OCF_{before}| \quad (2)$$

where OCF_{after} is obtained from the image of the filamentous network after rheology, and OCF_{before} is obtained from the image of the filamentous network before rheology. We have provided SEM images and corresponding orientation analysis of all other samples in Supplementary Information. (**Figure S9-S13**). The uncertainty in OCF derived from averaging over several images of biological triplicates is in the range $\pm$ 0.04 $-\pm$ 0.08 which is similar to the uncertainty deduced from Gaussian fitting (**Table 2**).

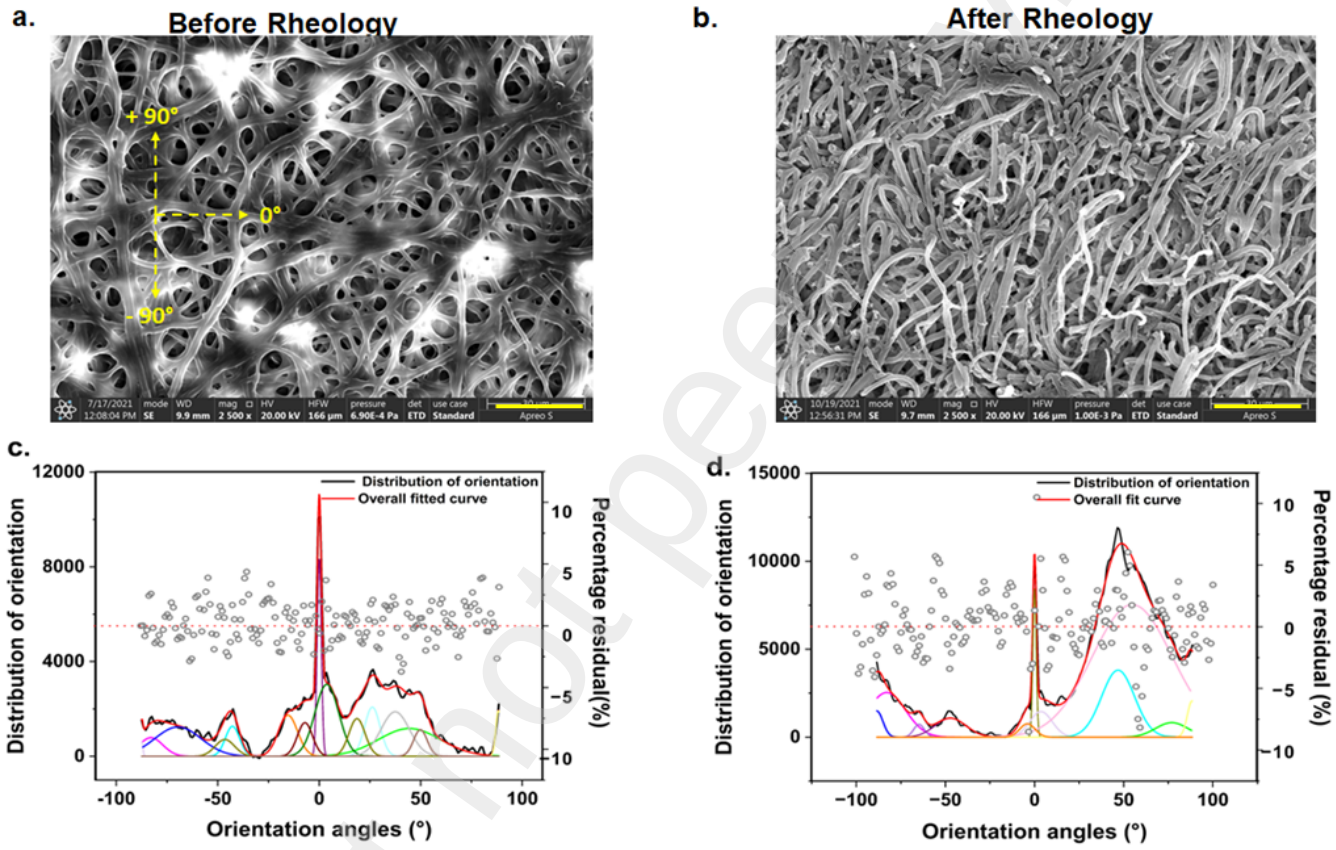

Figure 4. Orientation of filaments before and after rheology. Plots (a) and **(**b) show SEM images of the filaments oriented at different angles for the PC sample, as a representative of other biofilms, before and after rheology, respectively. The dashed lines (yellow color) define the reference orientations 0^0, $+90^0$, and -90^0. The scale bar (yellow color) is 30μm. Plots (c) and (d) show multiple Gaussian curves fitting the overall profile of filament orientation distribution derived from the SEM image. Open circles denote the fit residual, which varies between $\pm$ 5%.

4. Discussions

4.1. Correlation between nonlinear rheological property, extracellular matrix composition, and filament orientation of fungal biofilms

In this work, we influence the self-assembly of biofilms by regulating phosphorus and nitrogen in the growth reactor. The nutrients diffuse due to spatial gradients, determining the extent of the hyphal network, and the composition of EPS secreted by the filamentous cells. Thus, regulating the self-assembly of biofilms affects its rheology and microstructure. The universal scaling of the stress-strain plot (**Figure S7** a, b**)** before the yield strain suggests that three-dimensional short-range structural arrangement of the components of the biofilms is enough to explain their elastic solid-like behavior. However, to understand the nonlinear elastic behavior for $\gamma > \gamma_{ys}$signified by strain softening, shear thickening, and weak strain overshoot, we need (**Figure 1**a, b) to consider the nutrient-dependent chemical compositional variations of biopolymers in the EPS– the concentration of proteins and polysaccharides; and the distribution of orientation of filamentous cells.

Correlation of the intensity of the weak strain overshoot (β) with the biopolymer composition of biofilms

The protein and polysaccharide concentration for all the biofilms reported in our earlier study showed that nitrogen depletion increases the production of polysaccharides and proteins concentration per unit dry biomass. On the contrary, a decrease in phosphorus decreases the concentration of proteins and polysaccharides per unit dry biomass.[21] The polysaccharide content in these biofilms varies between 30% - 50% of the dry biomass (**Figure 5**). Recent studies, have shown similar high concentrations of polysaccharides produced in fungal biofilms.[57,58] A biofilm is a yield stress material with the strain overshoot peak acting like a barrier between a solid to a fluid-like state. Overall, the strain overshoot intensity, $\boldsymbol{\beta}$, decreases with nitrogen concentration and increases with phosphorous concentration (**Figure 5**). Interestingly $\boldsymbol{\beta}$ nearly follows the same trend as polysaccharides and protein concentrations per unit dry biomass (**Figure 5**) and can be considered as measure of the energy required to disrupt the extracellular polymer network. The Pearson correlation heatmap for the combined data of nitrogen and phosphorus trials show a statistically significant positive correlation between $\boldsymbol{\beta}$ and protein concentration (**Figure 7**). We believe that an effective crosslink between the matrix biopolymers and the hyphal network holds together the microstructure: It has contributions from the physical entanglement of polysaccharides, accessory proteins that reinforce the extracellular matrix,[32] electrostatic binding

due to multivalent cations in between two negatively charged polysaccharide polymers,[2] and the orientation of filaments. We can surmise that this effective crosslink is a potential barrier for the polymeric chains to move relative to each other. A similar study of the pectin-Ca gel system using LAOS showed that the intensity of the G" peak is related to the size of egg-box-shaped dimers formed due to calcium ions.[59] With an increase in shear strain amplitude, restructuring of the microstructure occurs, otherwise known as shear aging. For shear strain amplitudes beyond the G" peak, the polymer chains begin to flow past each other, causing shear thinning; this process where the microstructure cannot rebuild is known as shear rejuvenation in the parlance of yield stress materials.[60]

The intra-cycle indices *S* and *T* corroborate the link between the protein and polysaccharide concentrations and β. The magnitude of *S* and *T* values and their variation with strain is similar to physically and ionically crosslinked hydrogels.[52,59] In these fungal biofilms, the transition to $T > 0$ from $T = 0$ occurs for shear strains of about 3% (**Figure 3** c, d). In samples ND (0.044 g/L) and NA (0.7 g/L), which have relatively higher concentrations of protein and polysaccharide (**Figure 5**a), shear thickening occurs smoothly, compared to samples NB (0.35 g/L) and NC (0.175 g/L), which mildly shear thicken initially, and rapidly increase at higher shear strains. Shear thickening is attributed to the formation of temporary super-structures and entanglements whose size is estimated to be few tens of microns.[52] The polymer network is likely to have a higher density of 'junction points' at higher protein and polysaccharide concentrations. This should cause an increase in structural relaxation time reflected in increase in $\boldsymbol{\beta}$. NB and NC samples have relatively lower protein content per unit dry biomass and, therefore, have weaker crosslinks. The abrupt increase in *T*, around 30% shear strain, for these samples can be attributed to physical compaction.[32,61] Similarly, in the phosphorus trial, PC (0.282 g/L) shows weak thickening behavior and has the lowest protein concentration. In contrast, PA (1.13 g/L), which has the highest protein concentration among all the phosphorous trial samples, thickening begins over a larger range of shear strains (**Figure 5**b).

The intra-cycle elastic nonlinearities captured by the stiffening index *S* are also related to $\boldsymbol{\beta}$ and the EPS composition. Compared to nitrogen-trial biofilms, the phosphorous-trial biofilms have smaller $\boldsymbol{\beta}$, protein and polysaccharide concentrations; therefore, in phosphorous-trial biofilms, the transition to strain stiffening state ($S > 0$) is delayed and occur at higher shear strains (~ 40 %) (**Figure 4** a, b). Both enthalpic and entropic models are available to explain the nonlinear stiffening behavior in biomaterials.[62] The former attributes the transition to $S > 0$ to bending modes at low strains followed by stretching modes at higher strains. The present fungal biofilms

provide an additional challenge to these models as the deformation of the hyphal network has to be taken into account.

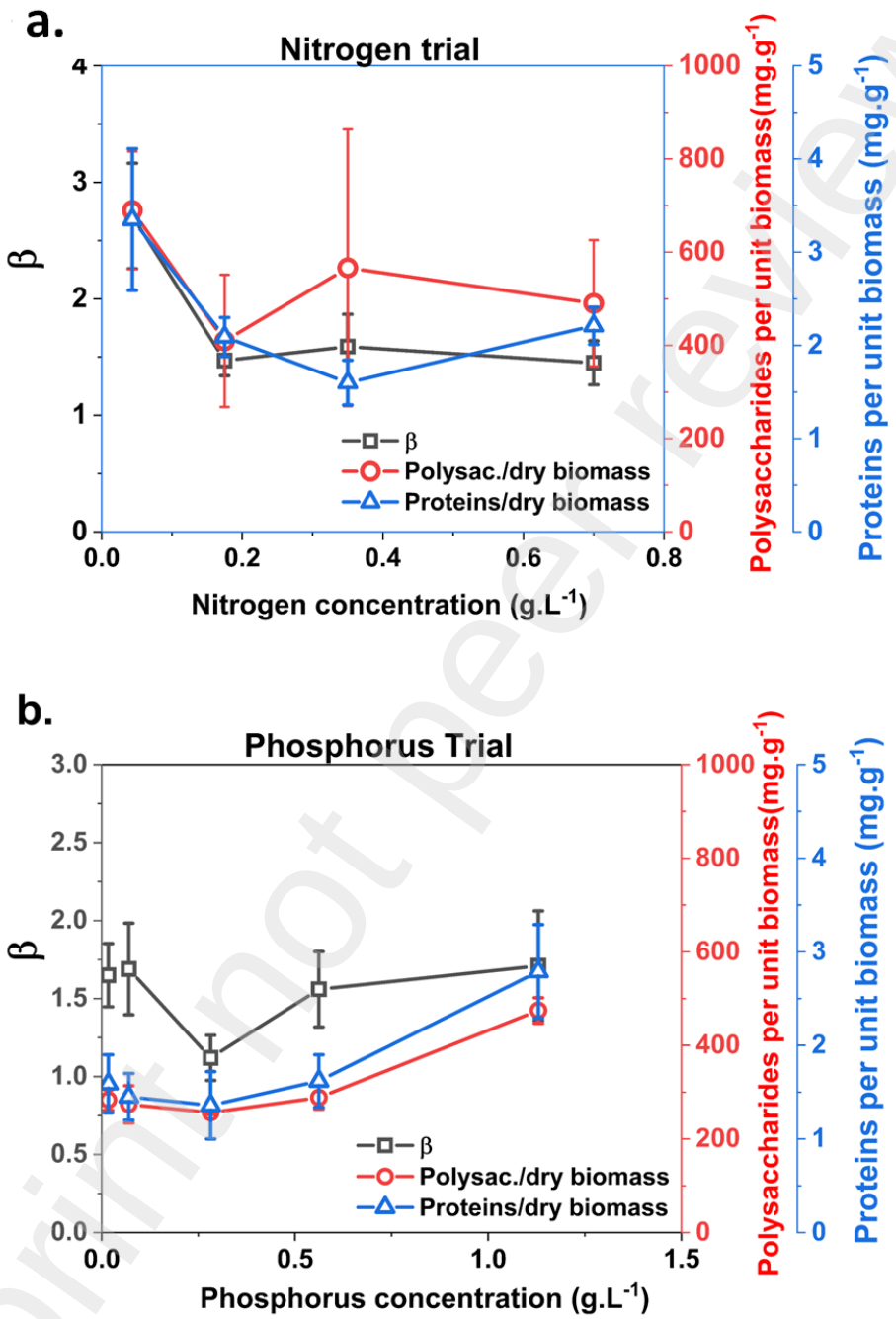

Figure 5. The dependence of intensity of weak overshoot $\boldsymbol{\beta}$ with biochemical composition of extracellular matrix. The proteins per unit biomass, polysaccharides per unit biomass, $\boldsymbol{\beta}$, are plotted as a function of (a) nitrogen concentration and (b) phosphorus concentration**.** Error bars correspond to one standard deviation (n=3).

Correlation of $\boldsymbol{\beta}$ with change in filament-orientation-complexity function

The directed hyphal network of fungal biofilms of *N. discreta* (**Figure 4**c) is akin to cellulose-based nematogels; their elastic modulus is comparable (~ kPa), and the orientational ordering of cellulose fibers have been shown to influence the physical properties [54]. F**igure 6** shows that biofilms grown under the lowest nitrogen concentration and the highest phosphorus concentration have the smallest $|\Delta(OCF)|$, and these biofilms have the highest $\boldsymbol{\beta}$ within the series. The plots $\boldsymbol{\beta}$ versus $\frac{1}{|\Delta(OCF)|}$ **(Figure 6**a, b) reveal an inverse relationship between $\boldsymbol{\beta}$ and $|\Delta(OCF)|$. The Pearson correlation heatmap for the combined data of nitrogen and phosphorus trials shows a statistically significant positive correlation between $\boldsymbol{\beta}$ and $|\Delta(OCF)|$ (**Figure 7**). A caveat on the statistical robustness of $|\Delta(OCF)|$ calculation is in order. We are comparing averaged data from the same annular region in the sample. Ideally, small-angle light scattering combined with oscillatory shear rheology would sample a larger area to provide a better estimate[63,64]. However, the challenge is improving the scattering contrast in these opaque biofilms.

Considering the non-crystalline structure of biofilms, we propose that filaments of different orientations and their distributions compete and jam to keep the biofilm in the elastic state. $|\Delta(OCF)|$, similar to $\boldsymbol{\beta}$ is proportional to the energy barrier between the elastic and plastic deformation state. The interpretation is that in biofilms with large $\boldsymbol{\beta}$, even after the yielding transition, there is minimal distortion in the filament orientation, compared to the mechanically unperturbed biofilm. Such biofilms possess robust filament architecture. The picture that emerges is that the extracellular matrix and the hyphal network dynamically interact with each other when subjected to LAOS (**Figure 8**). The extracellular proteins, which crosslink polymers in the extracellular matrix[32], could also similarly mediate between the filaments in the hyphal network, preventing them from altering their orientation. As we noted earlier, in the SAOS regime, the variations in protein concentrations do not affect the rheology of the biofilms. However, in the LAOS regime, the crosslinks are broken, and the polymer chains tend to align along the direction of deformation; this also implies an increase in the relative orientational disorder of the filaments.

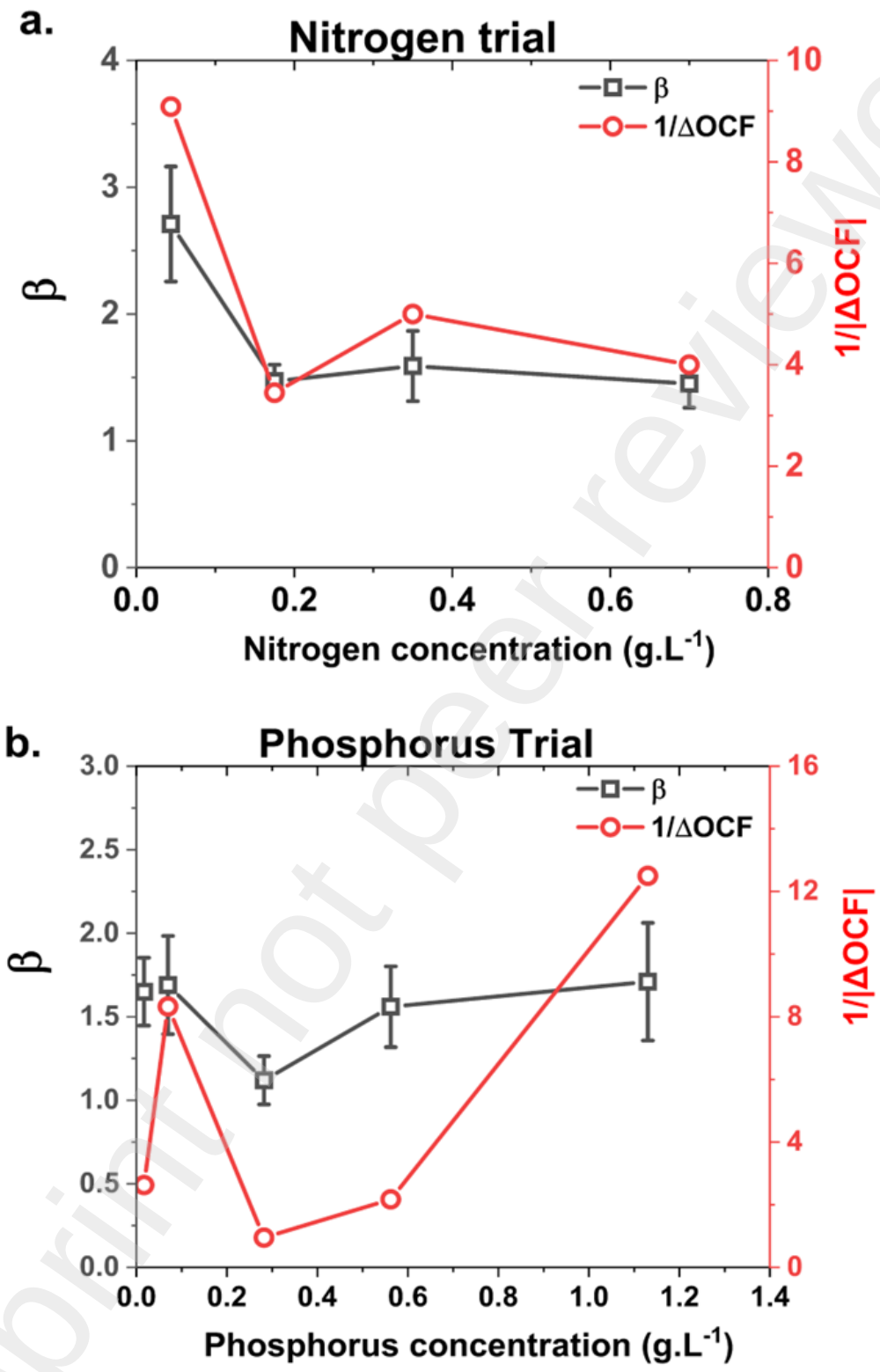

Figure 6. The correlation of the intensity of weak overshoot $\boldsymbol{\beta}$ with change in filament-orientation-complexity function $|\Delta OCF|$. $\boldsymbol{\beta}$, $1/(|\Delta OCF|)$, were plotted as a function of (a) nitrogen concentration and (b) phosphorus concentration. The error bar corresponds to one standard deviation (n=3). The uncertainty in $|\Delta OCF|$ corresponds to one standard deviation (**Table 2**).

Table 2. Filament-orientation-function (OCF) before and after shear deformation and intensity of strain overshoot ($\boldsymbol{\beta}$) for biofilms grown with varying nutrient concentrations. Errors correspond to one standard deviation.

Nutrient type	*Concentration* $(g.L^{-1})$	OCF_{before}	OCF_{after}	$\lvert\Delta OCF\rvert$	β
Nitrogen	0.700	1.73±0.07	1.48 ± 0.05	0.25 ± 0.09	1.45 ± 0.19
	0.350	1.56 ±0.07	1.36 ± 0.05	0.2 ± 0.09	1.59 ± 0.28
	0.175	1.56 ± 0.04	1.85 ± 0.08	0.29 ± 0.09	1.47 ± 0.13
	0.043	1.04 ± 0.02	1.15 ± 0.02	0.11 ± 0.03	2.71 ± 0.45
Phosphorus	1.130	1.49 ± 0.02	1.41 ± 0.06	0.08 ± 0.06	1.71 ± 0.35
	0.562	1.86 ± 0.03	1.34 ± 0.04	0.46 ± 0.05	1.56 ± 0.24
	0.282	2.45 ± 0.09	1.40 ± 0.11	1.05 ± 0.14	1.12 ± 0.14
	0.070	1.25 ± 0.02	1.37 ± 0.01	0.12 ± 0.02	1.69 ± 0.29
	0.017	1.74 ± 0.05	1.35 ± 0.04	0.38 ± 0.06	1.65 ± 0.20

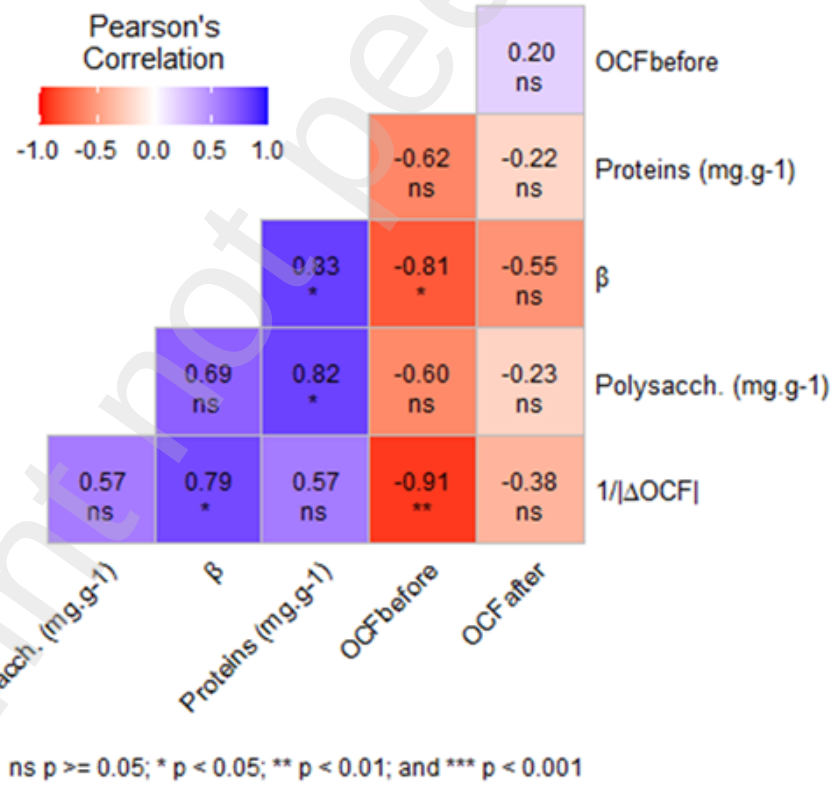

Figure 7. Pearson Correlation Heatmap: Combined (Nitrogen and Phosphorus trial) Pearson's correlation heat map depicting the relation between the biofilms' rheological and biochemical properties; OCF_{before}, OCF_{after}, $^{1}/_{|\Delta(OCF)|}$, $\boldsymbol{\beta}$, Polysaccharides per unit biomass ($mg.g^{-1}$), and Proteins per unit biomass ($mg.g^{-1}$). "no-significance (ns)'': p >= 0.05, "*'': $p < 0.05$, "**'': $p < 0.01$, "***'': $p < 0.001$

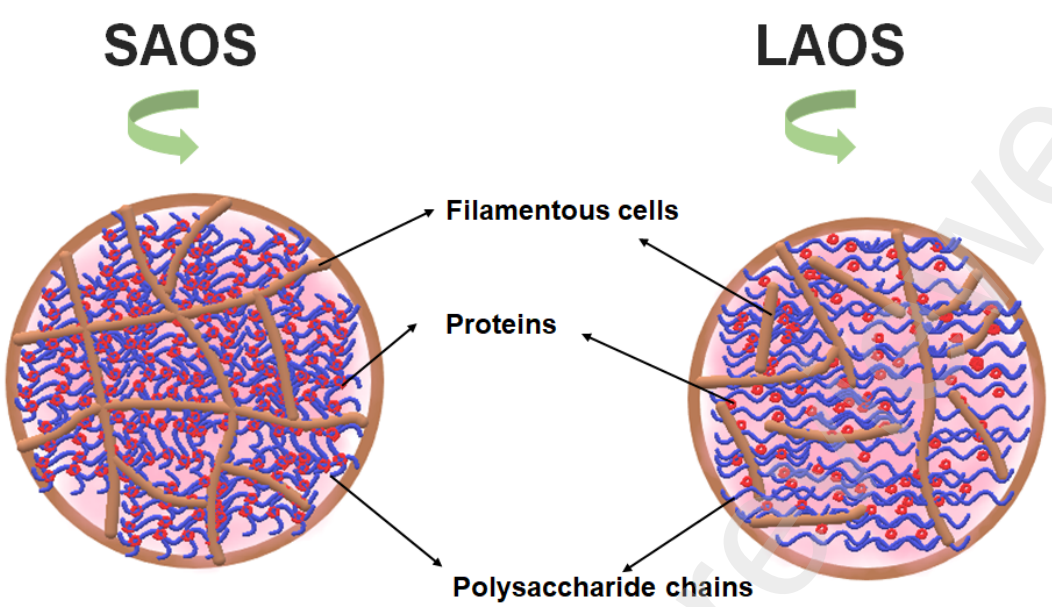

Figure 8. Schematic representation of coupled extracellular matrix and hyphal network. In the picture, the filaments are brown, red circles are the proteins, and blue chains represent the polysaccharides in the matrix. The left panel pertains to the picture of a biofilm in the SAOS regime, and the right panel corresponds to the same biofilms affected by large shear deformation.

5. Conclusion

Biofilm mechanics has been synonymous with structure-property correlations in bacterial biofilms. In this work, we investigated the non-linear viscoelastic behaviour of the less explored fungal biofilms. We used large amplitude shear rheology (LAOS) to study fungal biofilms of the filamentous fungus *Neurospora discreta*. These biofilms were grown by systematically regulating the amount of nitrogen and phosphorous in the growth media, which altered the composition of their extracellular polymeric substances (EPS) non-monotonically. Just as in many soft materials, we observed a peak in loss modulus (G") for strains between 30-50%, signifying a yielding transition from elastic to plastic deformation state. Our analysis suggests that the intensity in the peak in G" ($\boldsymbol{\beta}$) directly correlates with protein and polysaccharide concentrations present in the EPS. Intracycle strain stiffening and shear thickening indices reveal that the non-linear rheological behavior of the fungal biofilms originate from a viscous phenomenon, possibly due to the formation of temporary superstructures. We also find that the hyphal network resists mechanical deformation through minimal changes to the filament orientation. Overall, the results indicate a coupling of the extracellular polymer matrix and the hyphal network which could be exploited to tailor the mechanical properties of fungal biofilms.

Conflicts of interest

There are no conflicts of interest to declare

Data Availability

Data will be made available upon request.

References

1. Harrison, J. J., Turner, R. J., Marques, L. L., & Ceri, H. Biofilms: a new understanding of these microbial communities is driving a revolution that may transform the science of microbiology. Am. Sci. 93, 508–515 (2005).
2. Flemming, H. C. & Wingender, J. The biofilm matrix. Nat. Rev. Microbiol. 8, 623–633 (2010).
3. Hall-Stoodley, L., Costerton, J. W. & Stoodley, P. Bacterial biofilms: From the natural environment to infectious diseases. Nat. Rev. Microbiol. 2, 95–108 (2004).
4. Mattila-Sandholm, T. & Wirtanen, G. Biofilm Formation in the Industry: A review. Food Reviews International 8, 573-603 (1992).
5. Böl, M., Ehret, A. E., Bolea Albero, A., Hellriegel, J. & Krull, R. Recent advances in mechanical characterisation of biofilm and their significance for material modelling. Crit. Rev. Biotechnol. 33, 145–171 (2013).
6. Lieleg, O., Caldara, M., Baumgärtel, R. & Ribbeck, K. Mechanical robustness of Pseudomonas aeruginosa biofilms. Soft Matter 7, 3307–3314 (2011).
7. Boudarel, H., Mathias, J.-D., Blaysat, B. & Grédiac, M. Towards standardized mechanical characterization of microbial biofilms: analysis and critical review. npj Biofilms Microbiomes 4, 17 (2018).
8. Stoodley, P., Cargo, R., Rupp, C. J., Wilson, S. & Klapper, I. Biofilm material properties as related to shear-induced deformation and detachment phenomena. J. Ind. Microbiol. Biotechnol. 29, 361–367 (2002).
9. Hollenbeck, E. C. et al. Mechanical behavior of a Bacillus subtilis pellicle. J. Phys. Chem. B 120, 6080–6088 (2016).
10. Billings, N., Birjiniuk, A., Samad, T. S., Doyle, P. S. & Ribbeck, K. Material properties of biofilms - A review of methods for understanding permeability and mechanics. Reports Prog. Phys. 78, 036601 (2015).

11. Ünal Turhan, E., Erginkaya, Z., Korukluoğlu, M., Konuray, G. Beneficial Biofilm Applications in Food and Agricultural Industry. in Health and Safety Aspects of Food Processing Technologies 445–469 (Springer, 2019). doi:10.1007/978-3-030-24903-8.
12. Morikawa, M. Beneficial Biofilm Formation by Industrial Bacteria Bacillus subtilis and Related Species. J. Biosci. Bioeng. 101, 1–8 (2006).
13. Pamidipati, S. & Ahmed, A. Degradation of Lignin in Agricultural Residues by locally Isolated Fungus Neurospora discreta. Appl. Biochem. Biotechnol. 181, 1561–1572 (2017).
14. Harding, M. W., Marques, L. L. R., Howard, R. J. & Olson, M. E. Can filamentous fungi form biofilms? Trends Microbiol. 17, 475–480 (2009).
15. Morelli, K. A., Kerkaert, J. D. & Cramer, R. A. Aspergillus fumigatus biofilms: Toward understanding how growth as a multicellular network increases antifungal resistance and disease progression. PLoS Pathog. 17, 1–23 (2021).
16. Mazza, M. G. The physics of biofilms - An introduction. J. Phys. D. Appl. Phys. 49, 203001 (2016).
17. Cairns, T. C., Zheng, X., Zheng, P., Sun, J. & Meyer, V. Biotechnology for Biofuels Moulding the mould : understanding and reprogramming filamentous fungal growth and morphogenesis for next generation cell factories. Biotechnol. Biofuels 12, 77 (2019) doi:10.1186/s13068-019-1400-4.
18. Beckwith, J. K., Ganesan, M., VanEpps, J. S., Kumar, A. & Solomon, M. J. Rheology of Candida albicans fungal biofilms . J. Rheol. 66, 683–697 (2022).
19. Aravinda Narayanan, R. & Ahmed, A. Arrested fungal biofilms as low-modulus structural bio-composites: Water holds the key. Eur. Phys. J. E 42, 1-8 (2019).
20. Richardson, K. et al. Earth beyond six of nine planetary boundaries. Sci. Adv. 9, eadh2458 (2023).
21. Tabraiz, S., Aiswarya, N. M., Taneja, H., Narayanan, R. A. & Ahmed, A. Biofilm-based simultaneous nitrification, denitrification, and phosphorous uptake in wastewater by Neurospora discreta. J. Environ. Manage. 324, 116363 (2022).
22. Flemming, H. C. et al. The biofilm matrix: multitasking in a shared space. Nat. Rev. Microbiol. 21, 70–86 (2023).
23. Wilking, J. N., Angelini, T. E., Seminara, A., Brenner, M. P. & Weitz, D. A. Biofilms as complex fluids. MRS Bull. 36, 385–391 (2011).

24. Ahmed, A., Narayanan, R. A. & Veni, A. R. Influence of carbon source complexity on porosity, water retention and extracellular matrix composition of Neurospora discreta biofilms. J. Appl. Microbiol. 128, 1099–1108 (2020).
25. Zhang, W., Seminara, A., Suaris, M. & Brenner, M. P. Nutrient depletion in Bacillus subtilis biofilms triggers matrix production. New J. Phys. 16, 015028 (2014).
26. Needleman, D. & Dogic, Z. Active matter at the interface between materials science and cell biology. Nat. Rev. Mater. 2, 1-14 (2017).
27. Nagel, S. R. Experimental soft-matter science. Rev. Mod. Phys. 89, 025002 (2017).
28. Hyun, K. et al. A review of nonlinear oscillatory shear tests: Analysis and application of large amplitude oscillatory shear (LAOS). Prog. Polym. Sci. 36, 1697–1753 (2011).
29. Rogers, S. Large amplitude oscillatory shear: Simple to describe, hard to interpret. Phys. Today 71, 34 (2018).
30. Hyun, K., Kim, S. H., Ahn, K. H. & Lee, S. J. Large amplitude oscillatory shear as a way to classify the complex fluids. J. Nonnewton. Fluid Mech. 107, 51–65 (2002).
31. Jana, S. et al. Nonlinear rheological characteristics of single species bacterial biofilms. npj Biofilms Microbiomes 6, 19 (2020).
32. Zhang, Q. et al. Mechanical Resilience of Biofilms toward Environmental Perturbations Mediated by Extracellular Matrix. Advanced Functional Materials 32 2110699 (2022).
33. Charlton, S. G. V. et al. Microstructural and Rheological Transitions in Bacterial Biofilms. Adv. Sci. 2207373 (2023) doi:10.1002/advs.202207373.
34. Kamani, K., Donley, G. J. & Rogers, S. A. Unification of the Rheological Physics of Yield Stress Fluids. Phys. Rev. Lett. 126, 218002 (2021).
35. Donley, G. J., Singh, P. K., Shetty, A. & Rogers, S. A. Elucidating the G? overshoot in soft materials with a yield transition via a time-resolved experimental strain decomposition. Proc. Natl. Acad. Sci. U. S. A. 117, 21945–21952 (2020).
36. Charlton, S. G. V., Jana, S. & Chen, J. Yielding behaviour of chemically treated Pseudomonas fluorescens biofilms. Biofilm 8, 100209 (2024).
37. Geisel, S., Secchi, E. & Vermant, J. Experimental challenges in determining the rheological properties of bacterial biofilms. *Interface Focus* **12**, 20220032 (2022).
38. Ewoldt, R. H., Johnston, M. T. & Caretta, L. M. Experimental Challenges of Shear Rheology: How to Avoid Bad Data. in *Complex fluids in biological systems* 207–241 (Springer, 2014). doi:10.1007/978-1-4939-2065-5_6.
39. Irgens, F. *Rheology and Non-Newtonian Fluids*. (Springer International Publishing,

2014).

40. Abràmoff, M. D., Magalhães, P. J. & Ram, S. J. Image processing with ImageJ Part II. *Biophotonics Int.* **11**, 36–43 (2005).
41. Rezakhaniha, R. *et al.* Experimental investigation of collagen waviness and orientation in the arterial adventitia using confocal laser scanning microscopy. *Biomech. Model. Mechanobiol.* **11**, 461–473 (2012).
42. Savitzky, A. & Golay, M. J. E. Smoothing and Differentiation of Data by Simplified Least Squares Procedures. *Anal. Chem.* **36**, 1627–1639 (1964).
43. Läuger, J. & Stettin, H. Differences between stress and strain control in the non-linear behavior of complex fluids. *Rheol. Acta* **49**, 909–930 (2010).
44. Ewoldt, R., Winter, P. & McKinley, G. MITlaos User Manual Version 2.2 Beta for MATLAB. 21 (2008).
45. Wilhelm, M. Fourier-Transform Rheology. *Macromol. Mater. Eng.* **287**, 83 (2002).
46. Yang, K. & Yu, W. Dynamic wall slip behavior of yield stress fluids under large amplitude oscillatory shear. *J. Rheol.* **61**, 627–641 (2017).
47. Ewoldt, R. H., Hosoi, A. E. & McKinley, G. H. New measures for characterizing nonlinear viscoelasticity in large amplitude oscillatory shear. *J. Rheol.* **52**, 1427–1458 (2008).
48. Ong, E. E. S., O'Byrne, S. & Liow, J. L. Yield stress measurement of a thixotropic colloid. *Rheol. Acta* **58**, 383–401 (2019).
49. Yan, J. *et al.* Bacterial Biofilm Material Properties Enable Removal and Transfer by Capillary Peeling. *Adv. Mater.* **30**, 1–10 (2018).
50. Kovach, K. *et al.* Evolutionary adaptations of biofilms infecting cystic fibrosis lungs promote mechanical toughness by adjusting polysaccharide production. *npj Biofilms Microbiomes* **3**, 1 (2017).
51. Ewoldt, R. H. & McKinley, G. H. On secondary loops in LAOS via self-intersection of Lissajous-Bowditch curves. *Rheol. Acta* **49**, 213–219 (2010).
52. Goudoulas, T. B., Didonaki, A., Pan, S., Fattahi, E. & Becker, T. Comparative Large Amplitude Oscillatory Shear (LAOS) Study of Ionically and Physically Crosslinked Hydrogels. *Polymers (Basel).* **15**, 1558 (2023)
53. Chen, X. & Zhu, H. Predictive assembling model reveals the self-adaptive elastic properties of lamellipodial actin networks for cell migration. *Commun. Biol.* **3**, 616 (2020).
54. Liu, Q. & Smalyukh, I. I. Liquid crystalline cellulose-based nematogels. *Sci. Adv.* **3**,

e1700981 (2017).

55. Mclaughlin, J. C., Tagg, S. L. & Zwanziger, J. W. The Structure of Alkali Tellurite Glasses. *J. Phys. Chem. B* **105**, 67–75 (2001).
56. Ortiz-Burgos, S. Shannon-Weaver diversity index. U: Kennish MJ (ur.) Encyclopedia of estuaries. Encyclopaedia of Earth sciences series. 572–573 (2016).
57. Hou, S. J. *et al.* Improvement of extracellular polysaccharides production from Cordyceps militaris immobilized alginate beads in repeated-batch fermentation. *Lwt* **193**, 115752 (2024).
58. Li, F., Fan, H., Sun, Q., Di, Y. & Xia, H. Effects of Medium Additives on the Mycelial Growth and Polysaccharide Biosynthesis in Submerged Culture of Bjerkandera fumosa. *Molecules* **29**, (2024).
59. John, J., Ray, D., Aswal, V. K., Deshpande, A. P. & Varughese, S. Dissipation and strain-stiffening behavior of pectin-Ca gels under LAOS. *Soft Matter* **15**, 6852–6866 (2019).
60. Bonn, D., Denn, M. M., Berthier, L., Divoux, T. & Manneville, S. Yield stress materials in soft condensed matter. *Rev. Mod. Phys.* **89**, 1–40 (2017).
61. Kornet, R. *et al.* Less is more: Limited fractionation yields stronger gels for pea proteins. *Food Hydrocoll.* **112**, 106285 (2021).
62. Kang, H. *et al.* Nonlinear elasticity of stiff filament networks: Strain stiffening, negative normal stress, and filament alignment in fibrin gels. *Journal of Physical Chemistry B*, **113** 3799–3805 (2009).
63. Gilbert, P. H. & Giacomin, A. J. Small-angle light scattering in large-amplitude oscillatory shear. *Phys. Fluids* **31**, 103104 (2019).
64. Edera, P. *et al.* Deformation profiles and microscopic dynamics of complex fluids during oscillatory shear experiments. *Soft Matter* **17**, 8553–8566 (2021).

Supplementary Information

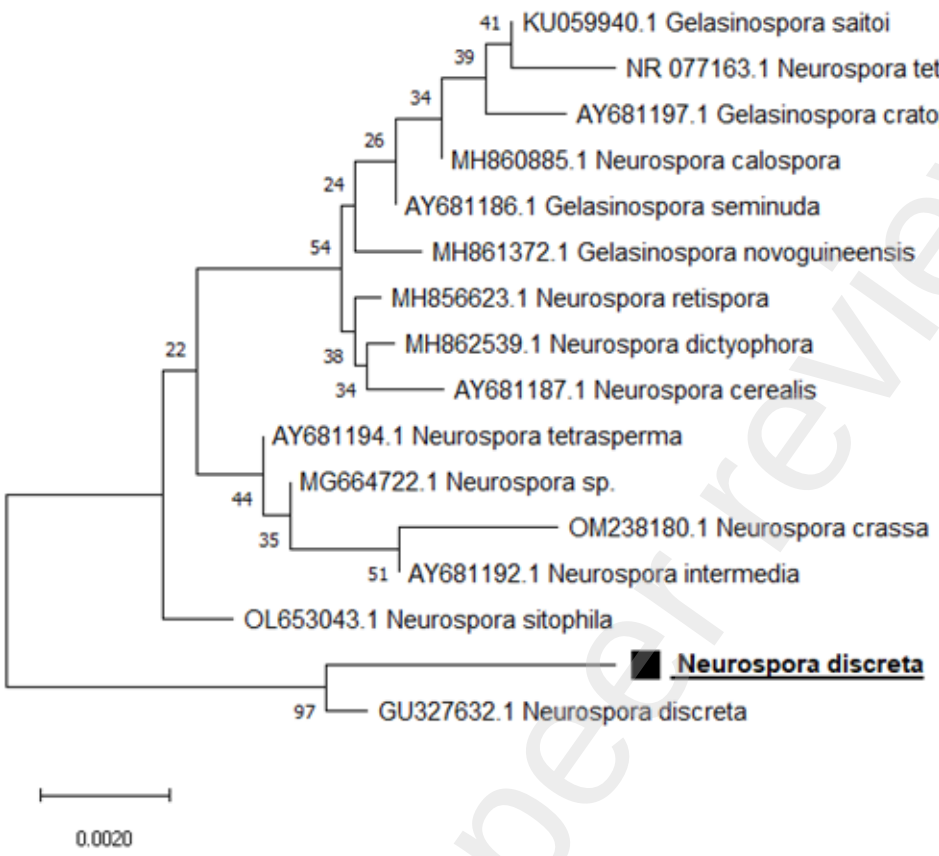

Figure S1. Neighbour – joining phylogenetic tree of fungus *Neurospora discreta.* The phylogenetic tree shows the internal transcribed spacer (ITS) gene sequence (bold and underlined) and 15 closest relatives, selected from a gene bank based on the ITS gene. Bootstrap values based on 100 replicates are displayed at the branches. The tree is drawn to scale, with branch lengths in the same units as those of the evolutionary distances used to infer the phylogenetic tree.

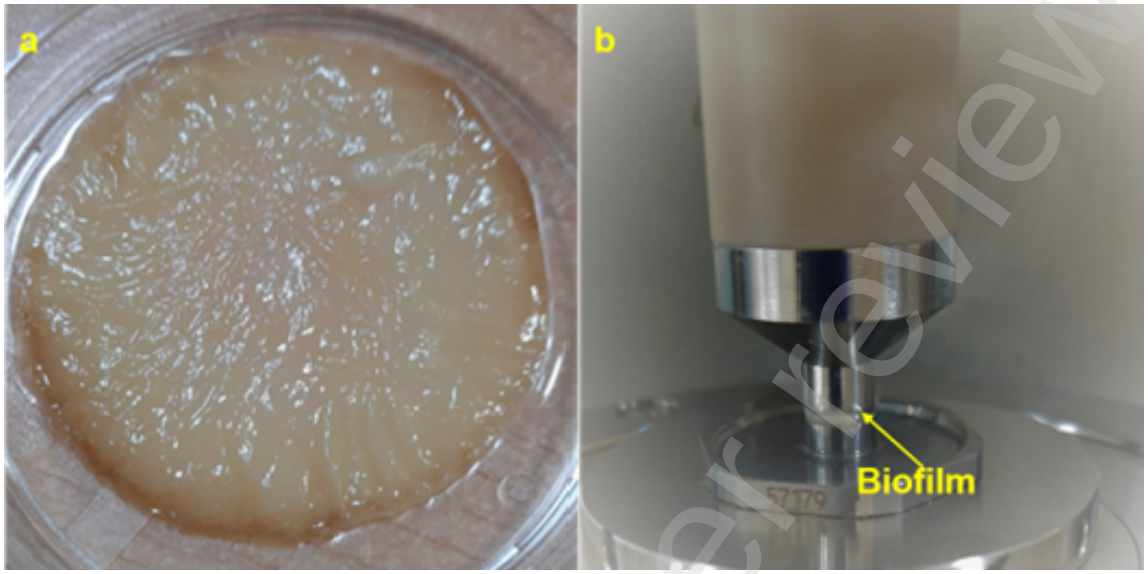

Figure S2. Macroscopic image of fungal biofilm. (a) Figure shows a typical biofilm produced by *Neurospora discreta* in laboratory after seven days of growth. (b) Figure shows an intact biofilm loaded between the parallel plates of the rheometer before performing LAOS tests.

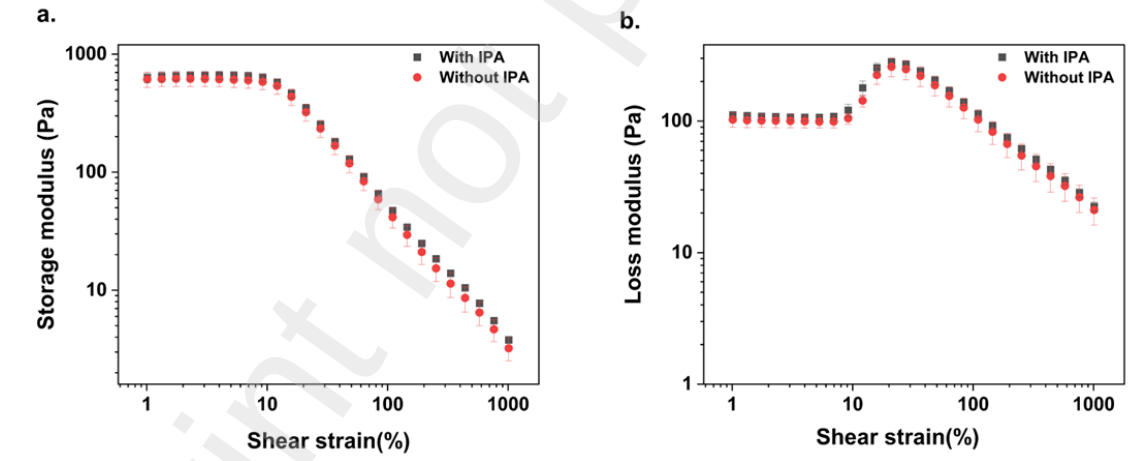

Figure S3. Storage modulus and loss modulus as a function of shear strain for xanthan gum 4wt% solution with and without isopropyl alcohol (IPA). The plot shows (a) storage modulus and (b) loss modulus.

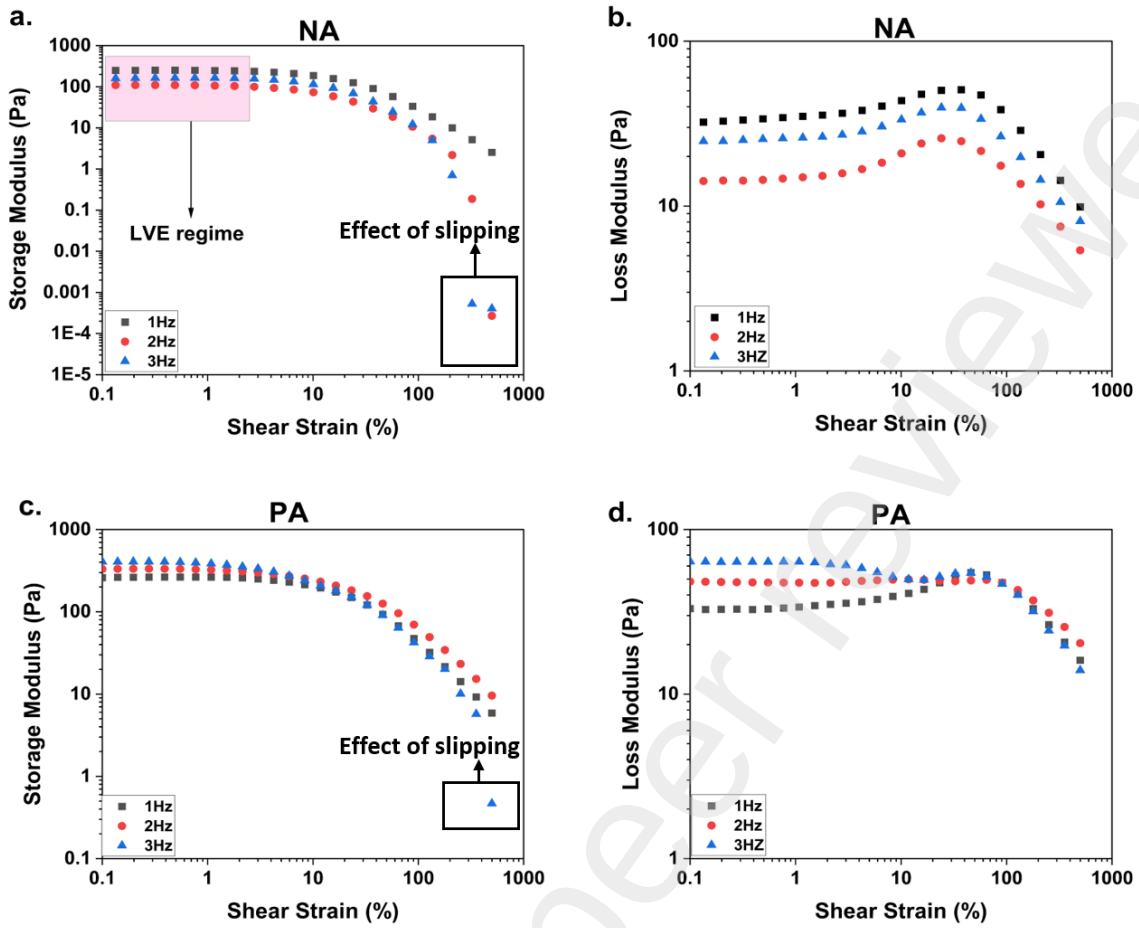

Figure S4. Storage modulus and loss modulus as a function of shear strain for different frequencies. The plot shows (a) storage modulus and (b) loss modulus for different frequencies for NA sample and (c) storage modulus and (d) loss modulus for different frequencies for PA sample.

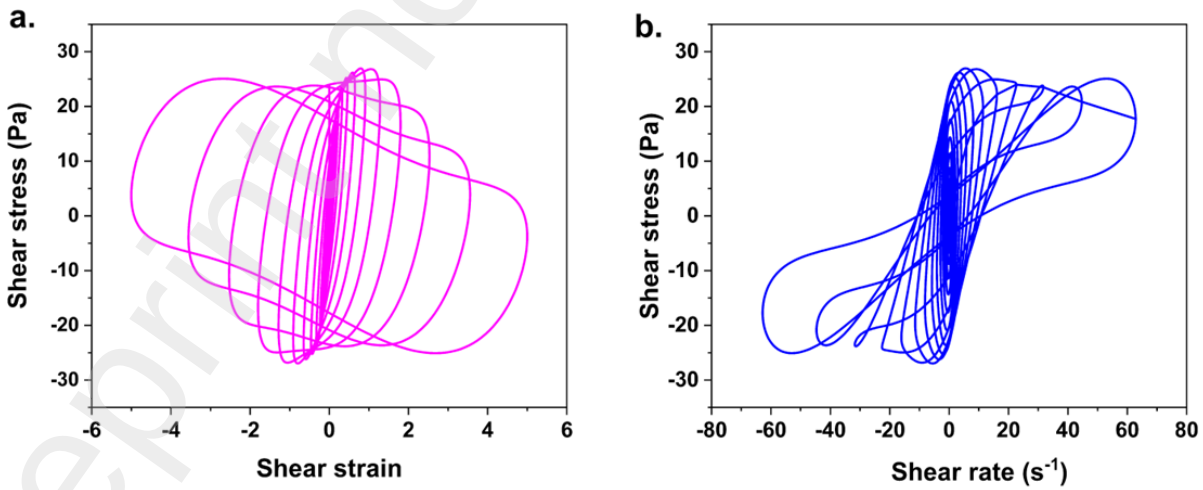

Figure S5. Slip effect on biofilms. The elastic and viscous Lissajous plots at higher strain and strain rates has the influence of instrument torque and causes slipping of the sample from the plates.

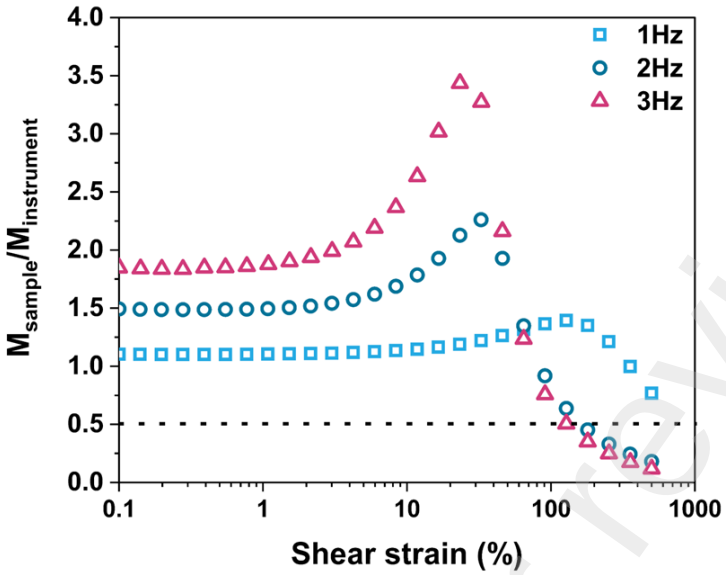

Figure S6. Torque ratio as a function of shear strain at different frequencies. The figure shows the variation of torque ratio for different frequencies. The dashed line corresponds to the cut-off ratio below which the data is not reliable

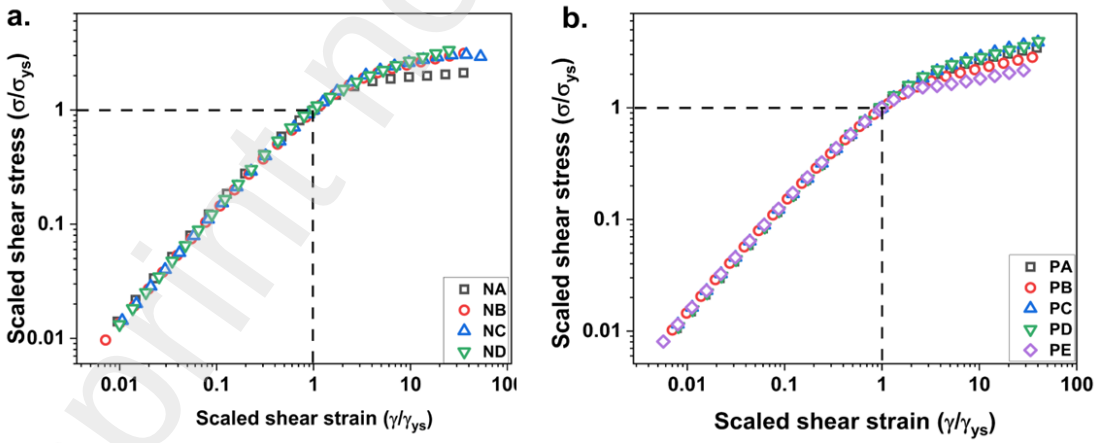

Figure S7. Scaled stress-strain shows nonlinear effects for larger strains. Shear stress and shear strain are scaled with respect to yield stress and yield strain, respectively and plotted for a) nitrogen trial and b) phosphorus trial.

Calibration of OrientationJ

We have created an image of predefined angles in MS Paint. Image consists 12 horizontal lines (0°), 22 vertical lines ($\pm$ 90°), 2 diagonal lines ($\pm$ 45°).

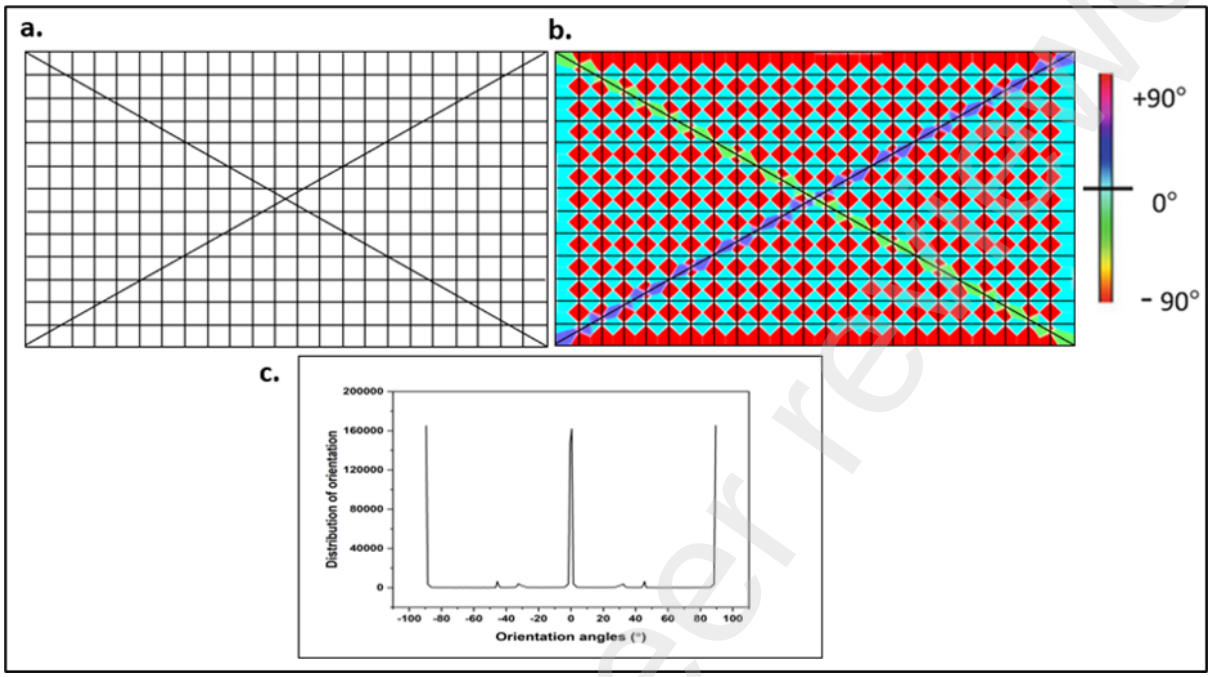

Figure S8. Summary of calibration of OrientationJ using an image with predefined angles. a) Image created in MS Paint, b) HSB coloured map of distribution of orientation obtained from OrientationJ Analysis to distinguish different angles, c) distribution of orientation obtained from OrientationJ Distribution

From **Figure S8** c, we can see peaks at $\pm 90°,\ \pm 45° and\ 0°$. However, we can also find small peaks $\pm 30°$ which are noise peaks

.

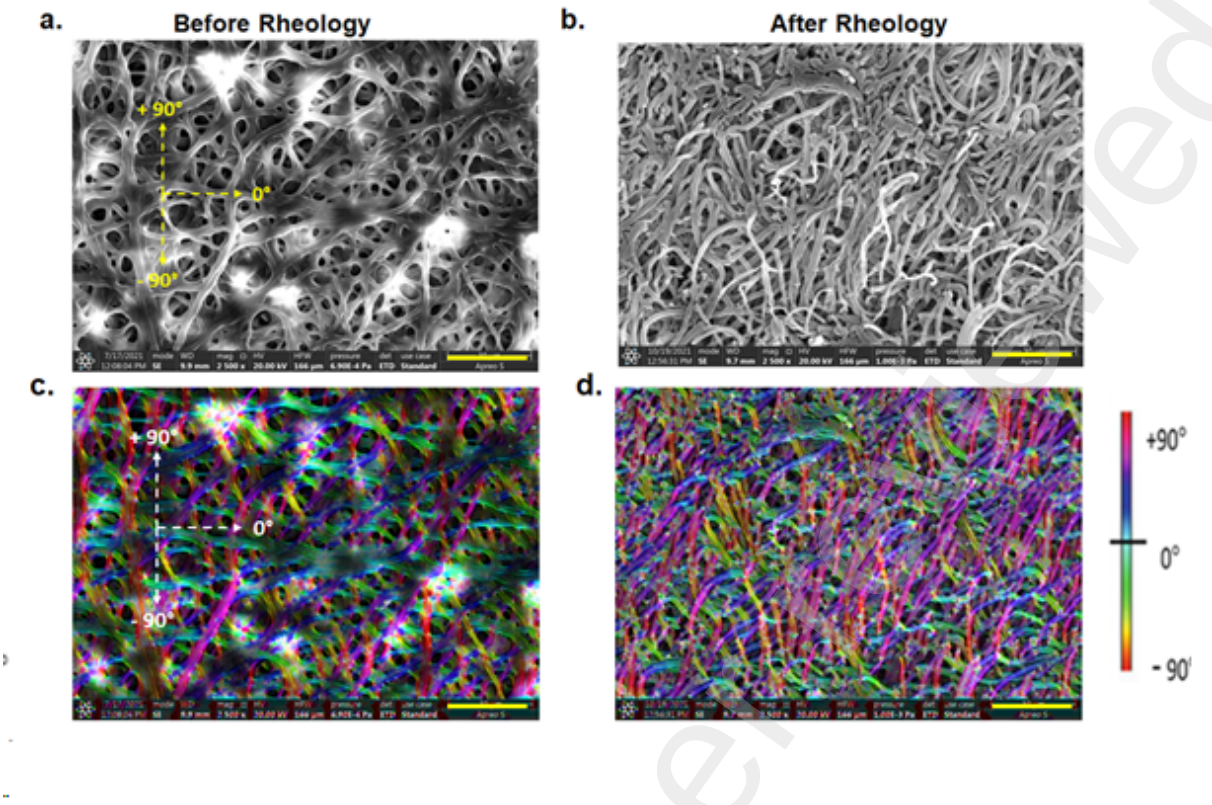

Figure S9. Orientation of filaments before and after rheology. Plots (a), (b) shows SEM image of the filaments oriented at different angles for the PC sample, as a representative of other biofilms, before and after rheology, respectively. The dashed lines (yellow colour) define the reference orientations, 0^0, $+90^0$, and -90^0. Plots (c), (d) shows HSB color-coded map of the SEM image of the orientation of filaments for the PC sample, as a representative of other biofilms, before and after rheology respectively. The dashed lines (white colour) define the orientations, 0^0, $+90^0$, and -90^0. The scale bar (yellow colour) is 30µm.

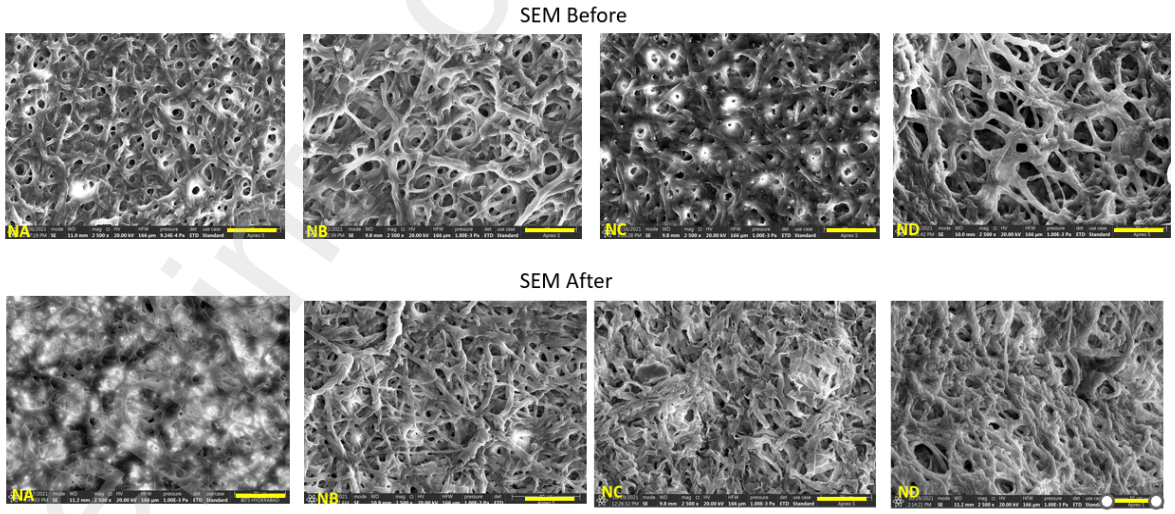

Figure S10. SEM images before and after deformation for nitrogen trial. Scale bar corresponds to *30µm*

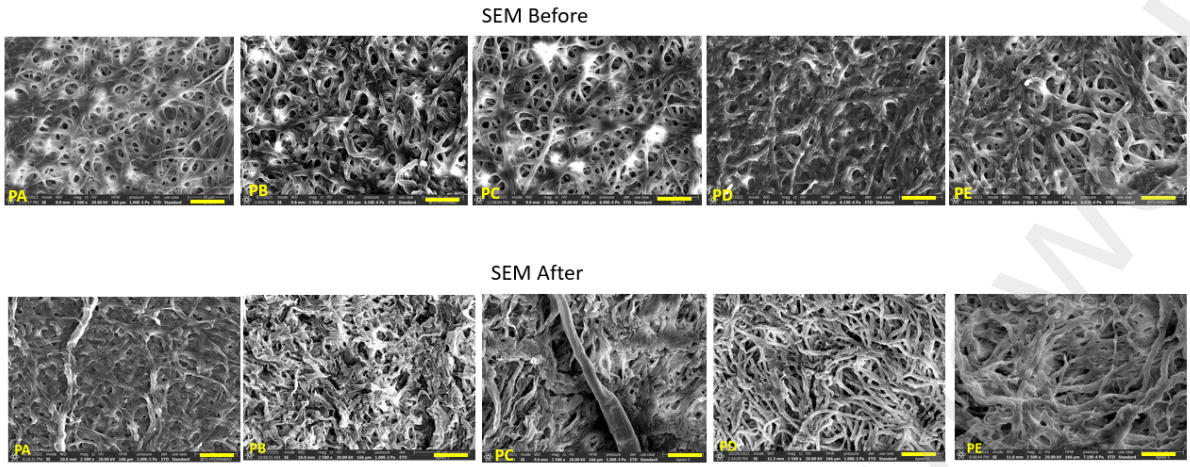

Figure S11. SEM images before and after deformation for phosphorus trial. Scale bar corresponds to *30μm*

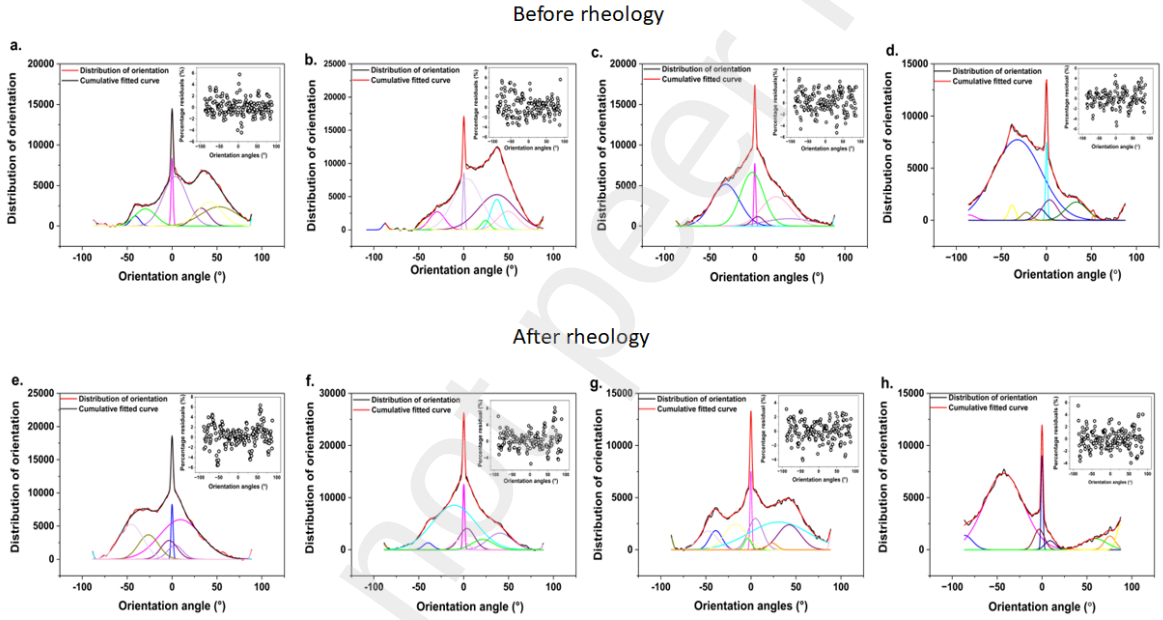

Figure S12. Orientation analysis results. (a-d) shows orientation analysis of nitrogen trial before rheology. Nitrogen concentration decreases from (a-d). The orientation analysis of nitrogen trial after rheology is shown in (e-h). Nitrogen concentration decreases from (e-h). Corresponding percentage residuals are given in inset.

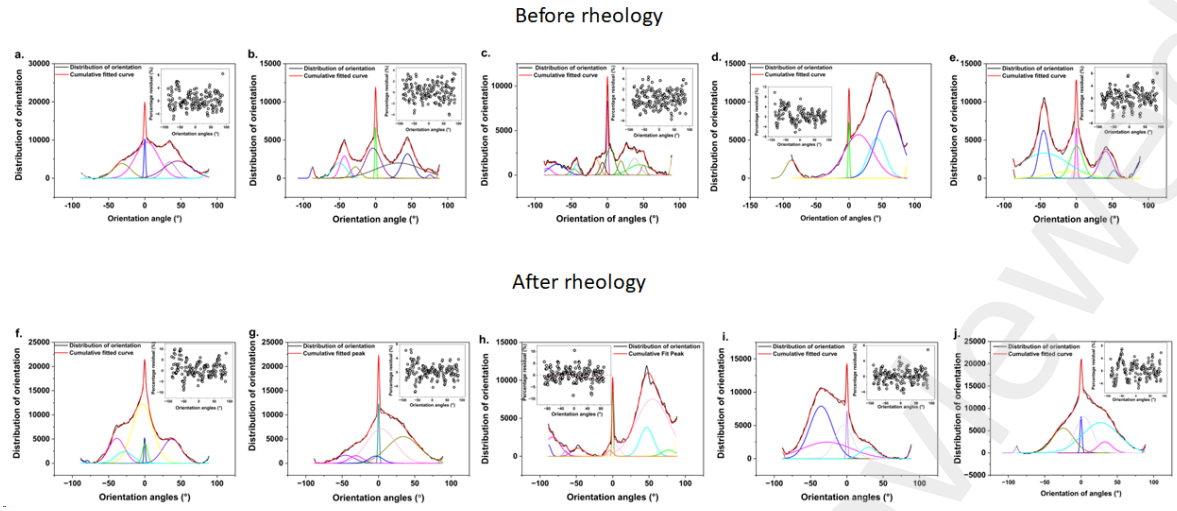

Figure S13. Orientation analysis results. (a-e) shows orientation analysis of phosphorus trial before rheology. Phosphorus concentration decreases from (a-e). The orientation analysis of phosphorus trial after rheology is shown in (f-j). Phosphorus concentration decreases from (f-j). Corresponding percentage residuals are given in inset.